Journal of Controlled Release 174 (2014) 63–71

Contents lists available at ScienceDirect

Journal of Controlled Release

journal homepage: www.elsevier.com/locate/jconrel

Hydrothermally synthesized PEGylated calcium phosphate nanoparticles incorporating Gd-DTPA for contrast enhanced MRI diagnosis of solid tumors

Peng Mi [a,b], Daisuke Kokuryo [c], Horacio Cabral [a], Michiaki Kumagai [d], Takahiro Nomoto [a], Ichio Aoki [c], Yasuko Terada [e], Akihiro Kishimura [f], Nobuhiro Nishiyama [b,*], Kazunori Kataoka [a,d,f,**]

[a] Department of Bioengineering, Graduate School of Engineering, The University of Tokyo, 7-3-1 Hongo, Bunkyo-ku, Tokyo 113–8656, Japan
[b] Polymer Chemistry Division, Chemical Resources Laboratory, Tokyo Institute of Technology, R1-11, 4259 Nagatsuta, Midori-ku, Yokohama 226–8503, Japan
[c] Molecular Imaging Center, National Institute of Radiological Sciences, Anagawa 4-9-1, Inage, Chiba, 263–8555, Japan
[d] Center for Disease Biology and Integrative Medicine, Graduate School of Medicine, The University of Tokyo, 7-3-1 Hongo, Bunkyo-ku, Tokyo 113–0033, Japan
[e] SPring 8, JASRI, 1-1-1 Kouto, Sayo-cho, Sayo-gun, Hyogo 679–5198, Japan
[f] Department of Materials Engineering, Graduate School of Engineering, The University of Tokyo, 7-3-1 Hongo, Bunkyo-ku, Tokyo 113–8656, Japan

ARTICLE INFO

Article history:
Received 18 July 2013
Accepted 28 October 2013
Available online 6 November 2013

Keywords:
Calcium phosphate nanoparticles
Block copolymer
Hydrothermal synthesis
MRI
Gd-DTPA
Cancer diagnosis

ABSTRACT

Organic–inorganic hybrid nanoparticles with calcium phosphate (CaP) core and PEGylated shell were developed to incorporate magnetic resonance imaging (MRI) contrast agent diethylenetriaminepentaacetic acid gadolinium (III) (Gd-DTPA) for noninvasive diagnosis of solid tumors. A two-step preparation method was applied to elaborate hybrid nanoparticles with a z-average hydrodynamic diameter about 80 nm, neutral surface ξ-potential and high colloidal stability in physiological environments by self-assembly of poly(ethylene glycol)-*b*-poly(aspartic acid) block copolymer, Gd-DTPA, and CaP in aqueous solution, followed with hydrothermal treatment. Incorporation into the hybrid nanoparticles allowed Gd-DTPA to show significant enhanced retention ratio in blood circulation, leading to high accumulation in tumor positions due to enhanced permeability and retention (EPR) effect. Moreover, Gd-DTPA revealed above 6 times increase of relaxivity in the nanoparticle system compared to free form, and eventually, selective and elevated contrast enhancements in the tumor positions were observed. These results indicate the high potential of Gd-DTPA-loaded PEGylated CaP nanoparticles as a novel contrast agent for noninvasive cancer diagnosis.

1. Introduction

Precise diagnosis of malignant tumors is essential for proper clinical treatments, and several diagnostic imaging methods have been applied. Among these, MRI can noninvasively provide highly quantitative and qualitative anatomical details of soft tissues [1]. In clinical, small paramagnetic molecules, especially Gd (III) based T_1 contrast agents are usually used for MRI measurements to improve the contrast of tissues, as the gadolinium complexes are stable and maintain strongly paramagnetic properties [2,3]. Nevertheless, tumor imaging using current clinically used contrast agents is often limited, because of their fast clearance from blood stream and low-tissue specificity, leading to inadequate sensitivity, specificity and spatial resolution [4]. Therefore, development of highly sensitive and tumor specific MRI probes has advocated much interest for cancer diagnosis. Accordingly, a myriad of nanoparticles have been considered as delivery carriers of contrast agents to optimize their pharmacokinetic properties for experimental or preclinical detection of solid tumors, such as polymeric micelles [5–10], liposomes [11,12], polymersomes [13,14], iron oxide nanoparticles [1,15,16], lipid nanoparticles [17–19] and other nanoscaffolds [20–23]. These nanoscale MRI probes have shown greater tumor selectivity than low molecular weight contrast compounds, owing to their ability to leak from the hyperpermeable vasculature of tumors and be retained in tumor tissues due to ineffective lymphatic drainage, which is known as the EPR effect [24]. Moreover, nanoscale MRI probes can provide higher sensitivity by increasing the relaxivity of the incorporated contrast agents due to decreased molecular tumbling rates [21,25,26]. In addition, they can combine their tumor imaging capability with cellular targeting and therapeutic activity by decorating the surface with ligands and incorporating bioactive molecules, respectively [27,28]. Development of efficient and safe nanocarriers for *in vivo* MR cancer detection could have a significant impact on human health care, owing to the widely clinical setting of MRI as well as the progressive increasing of cancer incidences all over the world [29].

* Correspondence to: N. Nishiyama, Polymer Chemistry Division, Chemical Resources Laboratory, Tokyo Institute of Technology, R1-11, 4259 Nagatsuta, Midori-ku, Yokohama 226–8503, Japan. Tel.: +81 45 924 5240; fax: +81 45 924 5275.
** Correspondence to: K. Kataoka, Department of Materials Engineering, Graduate School of Engineering, The University of Tokyo, 7-3-1 Hongo, Bunkyo-ku, Tokyo 113–8656, Japan. Tel.: +81 3 5841 7138; fax: +81 3 5841 7139.
E-mail addresses: nishiyama@res.titech.ac.jp (N. Nishiyama), kataoka@bmw.t.u-tokyo.ac.jp (K. Kataoka).

0168-3659/$ – see front matter © 2013 Elsevier B.V. All rights reserved.
http://dx.doi.org/10.1016/j.jconrel.2013.10.038

CaP-based drug delivery systems, firstly reported as carriers to enhance DNA transfection into mammalian cells before [30], attracted increasing interests in recent years because of its adequate biodegradation and excellent biocompatibility [31–34]. Many biochemical compounds can be incorporated in the solid framework of CaP nanoparticles to obtain improved functions. CaP nanoparticles can be prepared by various synthetic methods, including microemulsion [35,36], layer-by-layer [37,38] and wet chemical routes [39,40]. For some preparation procedures, it is usually difficult to control the crystal growth and the size of nanoparticles as well as prevent agglomeration. Moreover, for microemulsion synthetic route, which can achieve size control and colloidal stability, it is difficult to completely remove the synthetic precursors, especially some toxic agents like cyclohexane, and demulsification of nanoparticles may occur during purification [32].

We have pioneered the procedure to form PEGylated CaP nanoparticles with controlled size and appreciable colloidal stability by self-assembly in aqueous phase of CaP with PEG-polyanion block copolymers, such as poly(ethylene glycol)-*b*-poly(aspartic acid) (PEG-*b*-PAsp) [41]. In this way, organic–inorganic hybrid nanoparticles were formed with precise control of the growth of CaP crystal, as the anionic blocks of the copolymers interact with CaP inhibiting further growth of crystal, while PEG units decorate the surface of nanoparticles avoiding aggregation between CaP particles [42–44]. This PEG shield also protects the drug-loaded core during transportation in biological environments. By this method, we have successfully incorporated small interfering RNA (siRNA) or DNA inside CaP hybrid nanoparticles as non-viral gene carriers and achieved efficient transfection efficiency, demonstrating promising application for gene therapy [45–47]. Nevertheless, it is a challenge to load some functional molecules, such as Gd-DTPA, without phosphate groups like siRNA and DNA, to interact with CaP matrix. Besides, high colloidal stability of nanoscale probes for MRI is preferred, as leaking of contrast agents during transportation may lose contrast specificity, and Gd-DTPA has a blood half-time less than 5 min which is insufficient to enhance the contrast of tumor tissues [48]. Thus, developing stable CaP nanoparticles incorporating Gd-DTPA for cancer diagnosis is quite challenging and significant, as CaP based nanocarriers for *in vivo* MRI diagnosis of solid tumors have not been reported yet.

Herein, we designed a facile two-step method to prepare organic–inorganic hybrid CaP nanoparticles stably incorporating Gd-DTPA (Gd-DTPA/CaP) with enhanced relaxivity and physiological stability for noninvasive *in vivo* cancer diagnosis (Fig. 1). Accordingly, spherical and monodispersed Gd-DTPA/CaP were firstly synthesized by a fast homogenous procedure using PEG-*b*-PAsp to prevent the overgrowth of CaP precipitates. Then, Gd-DTPA/CaP was subjected to hydrothermal synthetic process at relatively low temperature of 120 °C to increase the colloidal stability, as hydrothermal treatment is usually used to treat hydroxyapatite materials for orthopedics applications to enhance its mechanical reliability (stability) in wet environments [49]. Prepared Gd-DTPA/CaP was characterized by a series of *in vitro* and *in vivo* experiments, and further used for *in vivo* MRI contrast enhancement of solid tumors.

2. Materials and methods

2.1. Materials, cell line and animals

β-Benzyl-L-aspartate *N*-carboxy-anhydride (BLA-NCA) was obtained from Chuo Kaseihin Co., Inc. (Tokyo, Japan). Dulbecco's Modified Eagle Medium (DMEM), fetal bovine serum (FBS) and Gd-DTPA were purchased from Sigma–Aldrich (St. Louis, Missouri). Gd-DTPA was converted to sodium salt by adjusting the pH to 7 with NaOH and lyophilizing before use. MeO-PEG-NH_2 (Mw = 12,000, Mw/Mn = 1.03) was purchased from Nippon Oil and Fats Co., Ltd. (Tokyo, Japan).

Murine colon adenocarcinoma 26 (C-26) cells were kindly supplied by the National Cancer Center (Tokyo, Japan), and maintained with DMEM supplemented with 10% FBS. Human umbilical vein endothelial cells (HUVEC) and the endothelial cell growth medium-2 (EGM-2) bullet kit were obtained from Lonza Ltd. (Basel, Switzerland). The HUVEC were used for experiments after 10 times passage. All the cells were maintained in the medium and incubated in humidified atmosphere containing 5% CO_2 at 37 °C. Female BALB/c nude mice (6 weeks, 18–20 g) were purchased from Charles River Laboratories, Inc. (Tokyo, Japan), and all the animal experiments were carried out following the policies of the Animal Ethics Committee of the University of Tokyo.

2.2. Synthesis of PEG-b-PAsp

PEG-*b*-PAsp block copolymer with 40 degree of polymerization (DP) for PAsp was synthesized according to the previously described synthetic methods [50]. Briefly, BLA-NCA was polymerized by ring-opening procedures in mixed solvent of DMF and CH_2Cl_2, initiated by the primary amino group of MeO-PEG-NH_2 (M_w = 12,000) to obtain PEG-*b*-poly (β-benzyl-L-aspartate) (PEG-*b*-PBLA) block copolymer. The molecular weight distribution of PEG-*b*-PBLA was M_w/M_n = 1.05, which was determined by gel permeation chromatography (GPC) system (HLC-8220, Tosoh, Japan) equipped with TSK-gel columns (SuperAW3000 and SuperAW4000, Tosoh Bioscience LLC, Tokyo, Japan) and an internal refractive index (RI) detector at 40 °C. *N*-methyl-2-pyrrolidone (NMP) containing LiBr (50 mM) was used as mobile phase and linear PEG standards were used for calibration. The DP was determined to be 40 by

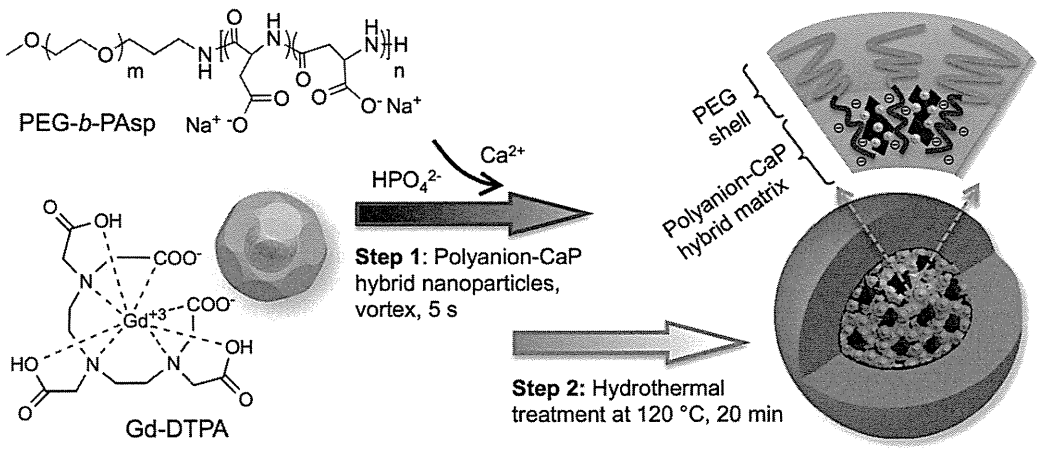

Fig. 1. Scheme showing the design and synthetic procedures of developing Gd-DTPA doped, PEG-*b*-PAsp hybrid calcium phosphate nanoparticles (Gd-DTPA/CaP) following a two-step method of PEG-polyanion controlled preparation in 5 s and hydrothermal treatment at 120 °C for 20 min to enhance the colloidal stability of nanoparticles.

comparing the proton ratios of methylene units in PEG (–OCH_2CH_2–: $\delta = 3.7$ ppm) and phenyl groups of PBLA (–C_6H_5: $\delta = 7.3$ ppm) in ^{1}H-NMR measurement (solvent: DMSO-d_6, temperature: 80 °C). PEG-*b*-PAsp (12 k-40DP) was obtained via removing benzyl groups of PEG-*b*-PBLA, which was carried out by mixing with 0.5 N NaOH (5 eq.) at room temperature and reacted for 1 h, then the block copolymer was dialyzed against Mili-Q water, and finally collected by lyophilization. The deprotection was confirmed by ^{1}H-NMR measurement (solvent: D_2O, temperature: 25 °C).

2.3. Fabrication of Gd-DTPA/CaP

Firstly, 0.1 ml of 2.5 M $CaCl_2$ was diluted in 1 ml Tris–HCl buffer (pH 7.6) (solution A). PEG-*b*-PAsp at the concentration of carboxylic acid groups of PAsp from 3 mM to 6 mM respectively, and Gd-DTPA at a concentration of 2 mM were dispersed in 50 mM HEPES saline buffer (pH 7.1, NaCl 140 mM) containing 6 mM Na_2HPO_4 (solution B). Equal volume of solution B was quickly added to solution A with vigorous stirring by a vortex mixer for 5 s. Then, Gd-DTPA/CaP nanoparticles were treated by hydrothermal synthesis for 20 min at 120 °C using an autoclave machine under the pressure of 100 kPa. The hydrothermal treated Gd-DTPA/CaP nanoparticles were purified by dialysis and ultrafiltration (MWCO: 100,000) using 25 mM HEPES saline buffer (pH 7.4, NaCl 140 mM and 2 mM $CaCl_2$). Gd-DTPA/CaP nanoparticles without hydrothermal treatment were also purified as above described as control.

2.4. Characterization of Gd-DTPA/CaP

Size distribution of obtained Gd-DTPA/CaP nanoparticles was evaluated by dynamic light scattering (DLS) measurement using a Zetasizer Nano ZS90 (Malvern Instruments, UK). The amount of Gd-DTPA incorporated in CaP nanoparticles was determined by ICP-MS (4500 ICP-MS, Hewlett Packard, Delaware, USA). Then, 1 ml of Gd-DTPA/CaP nanoparticles was lyophilized and the weight was measured to calculate the loading efficacy. Meanwhile, 1 ml of Gd-DTPA/CaP nanoparticles was dialyzed (MWCO: 6000–8000) in 5 L of Mili-Q water and the water was changed for several times. The existence of nanoparticles was checked by DLS and, 72 h later, the inner solution of dialysis bag was lyophilized and the weight was measured to calculate the composition of block copolymer. The morphology of Gd-DTPA/CaP nanoparticles was investigated using TEM (JEM-1400, JEOL, Tokyo, Japan). The hydroxyapatite crystal line of the obtained product was characterized by X-ray diffraction (XRD) (PW18v5/20, Philips, Amsterdam, Netherlands) with Cu-Kα incident radiation. The proton longitudinal relaxation rate r_1 of Gd-DTPA/CaP and Gd-DTPA was measured in 10 mM PBS buffer (pH 7.4, NaCl 140 mM) at 37 °C by utilizing ^{1}H-NMR analyzer (JNM-MU25A, JEOL, Tokyo, Japan) at 0.59 T. The longitudinal relaxation time T_1 (s) was measured by inversion-recovery pulse sequence method. The T_1 (s) values of 0.2, 0.4, 0.6, 0.8 and 1.0 mM Gd-DTPA and Gd-DTPA/CaP were measured and the r_1 relaxivity was calculated from the equation of $r_1 = (1/T_1 - 1/T_{1(0)})/[Gd]$, where [Gd] is the concentration of paramagnetic CAs (mM), $1/T_{1(0)}$ (s^{-1}) is the longitudinal relaxation rate contrast in the absence of a paramagnetic species, and $1/T_1$ (s^{-1}) is the longitudinal relaxation rate contrast in the presence of a paramagnetic species. Moreover, equal volume of solutions containing 0.1, 0.2, 0.3 and 0.4 mM Gd-DTPA or Gd-DTPA/CaP in saline buffer were placed in thin-wall PCR tubes, respectively, and then closed with flat caps for MR imaging at 1 T (Aspect, Aspect Imaging).

2.5. Physicochemical characterization

Gd-DTPA released from Gd-DTPA/CaP was measured by dialysis of Gd-DTPA/CaP in 10 mM PBS buffer (pH 7.4, NaCl 140 mM) incubated at 37 °C with shaking. One-tenth milliliter of outer solution was sampled at defined time, and the concentration of Gd-DTPA was measured by ICP-MS. To study the stability of Gd-DTPA/CaP, the samples were washed with methanol to remove free Ca^{2+} ions in the buffer by ultrafiltration, and finally washed with 10 mM PBS buffer (pH 7.4, NaCl 140 mM). Then, samples were incubated in physiological environments (10 mM PBS buffer containing 140 mM NaCl, pH 7.4 and 37 °C) and characterized by DLS and static light scattering (SLS) using a Photal dynamic laser light scattering spectrophotometer (Photal DLS-7000, Otsuka Electronics). The ξ-potential of Gd-DTPA/CaP nanoparticles was measured in 10 mM phosphate buffer (pH 7.4) using Zetasizer Nano ZS90.

2.6. Cytotoxicity study

To determine the cytotoxicity of Gd-DTPA/CaP and Gd-DTPA, HUVEC and C-26 cells were seeded in 96 well plates and incubated respectively. Twenty-four hours later, the cells were exposed to free Gd-DTPA or Gd-DTPA/CaP for 72 h, followed by adding Cell Counting Kit-8 solution (Dojindo Molecular Technologies, Inc., Japan). The cell viability in each plate was measured using a micro-plate reader (Model 680, Bio-Rad Laboratories, Inc., Hercules, US) at 450 nm.

2.7. In vivo biodistribution assay

Female BALB/c nude mice were inoculated subcutaneously with 100 μl of C-26 tumor cells at a concentration of 1×10^6 cell/ml to prepare subcutaneous tumor models. When the subcutaneous tumor volume reached 100 mm^3, Gd-DTPA/CaP and free Gd-DTPA were intravenously injected to C-26 tumor-bearing mice at a dose of 0.02 mmol/kg based on Gd-DTPA. Then, tumor and major organs were harvested at 1, 4, 8 and 24 h. Meanwhile, blood was collected from the inferior vena cava, heparinized and centrifuged to obtain the plasma. The plasma and all organs were dissolved in 90% HNO_3, evaporated and re-dissolved in 1% HNO_3 solution to prepare samples for ICP-MS measurement. Moreover, equal dose of Gd-DTPA and Gd-DTPA/CaP was intravenously injected to C-26 subcutaneous tumor-bearing mice. The tumor tissues were harvested, immediately put into OCT compound, and then frozen in acetone/dry ice mixture. The frozen samples were further cut to 16-μm thickness in a cryostat (CM1950, Leica, Germany). Next, some sections were fixed and stained with hematoxylin and eosin (H&E) and then samples were observed by using an AX80 microscope (Olympus, Japan). Other tumor tissue sections were scanned by micro-synchrotron radiation-induced X-ray fluorescence spectrometry (μ-SR-XRF) using beamline 37XU in SPring-8 (Hyogo, Japan) with 14 keV of energy and an intensity of 1×10^{12} photons per second to determine distributions of Gd, Ca and Fe elements in tumor sections [51].

2.8. MRI measurements

BALB/c nude mice (female, 6 weeks) were inoculated subcutaneously with C-26 cells to prepare tumor models for MRI measurements. *In vivo* MR imaging of the tumors was conducted with a 1 T imaging spectrometer (Aspect, Aspect Imaging) until the mean tumor volume reached 100 mm^3. Gd-DTPA/CaP was intravenously injected to C-26 subcutaneous tumor bearing mice at a dose of 0.05 mmol/kg based on Gd-DTPA for MRI imaging with anesthesia, while *in vivo* MRI administrated with Gd-DTPA at a dose of 0.22 mmol/kg was measured as control. For the T_1-weighted MR imaging of live mice, the following parameters were adopted: spin-echo method, repetition time (TR) = 400 ms, echo time (TE) = 11 ms, field of view (FOV) = 48 × 48 mm, matrix size = 256 × 256, and slice thickness = 2 mm.

Table 1
Size and distribution of Gd-DTPA/CaP nanoparticles measured by DLS.

Concentration of COO^- from PEG-*b*-PAsp (mM)[a]	Z-average diameter (nm)	Polydispersity index (PDI)
3	565 ± 19	0.59 ± 0.04
4	190 ± 16	0.26 ± 0.03
5	76 ± 10	0.14 ± 0.02
6	78 ± 6	0.17 ± 0.02

[a] The concentration of Gd-DTPA was fixed at 2 mM.

3. Results and discussion

3.1. Fabrication and characterization of Gd-DTPA/CaP nanoparticles

For *in vivo* applications, homogeneous and small sizes of CaP nanoparticles are preferred, while a PEGylated surface increases the biocompatibility of nanoparticles. To achieve this, a simple two-step method was adopted for preparing Gd-DTPA/CaP nanoparticles. In the first homogenous preparation step, Gd-DTPA/CaP nanoparticles were prepared by mixing Tris–HCl solution containing 250 mM Ca^{2+} and HEPES solution containing 6 mM HPO_4^{2+}, 2 mM Gd-DTPA and varying concentration of PEG-*b*-PAsp block copolymer with vigorous shaking using vortex mixer. Considering stability of CaP prepared at room temperature was not high [52], we treated the solution of Gd-DTPA/CaP nanoparticles at 120 °C for 20 min under a pressure of 100 kPa for hydrothermal treatment to increase their colloidal stability. Hydrothermal treatment at elevated temperature and pressure is often used to modulate the properties of inorganic materials, for instance, to treat hydroxyapatite based biomaterials for orthopedic applications to increase the crystallinity, thereby improving the mechanical reliability in wet environments [49,52,53].

As shown in Table 1, increase in the concentration of carboxylic acid groups of PEG-*b*-PAsp from 3 mM to 6 mM caused dramatic decrease in the hydrodynamic diameter of Gd-DTPA/CaP from over 565 nm to sub-100 nm while reducing polydispersity index (PDI). This trend was maintained until the nanoparticles reached approximately 76 nm using 5 mM carboxylate solution of PEG-*b*-PAsp (Fig. 2A). Hydrothermal treatment induces no significant change in the size and PDI of Gd-DTPA/CaP samples, and there was only a very slight increase in the average size to 80 nm after purification. Then, freeze-dried sample of Gd-DTPA/CaP nanoparticles with hydrothermal treatment was analyzed by X-ray diffraction pattern (XRD) measurement, and typical peaks of hydroxylapatite crystal were found (Fig. 2B), demonstrating the existence of $Ca_{10}(PO_4)_6(OH)_2$ [49,52]. Inside Gd-DTPA/CaP nanoparticles, the organic parts (block copolymer and Gd-DTPA) composed up to near 30% (weight/weight) and the content of Gd-DTPA was approximately 2.5% of the whole weight.

The Gd-DTPA/CaP samples obtained without hydrothermal treatment were not stable even during purification procedures (dialysis and ultrafiltration). Size evaluation by DLS gave a broad size distribution and some of those nanoparticles were broken according to TEM image shown in Fig. 2C. The morphology of Gd-DTPA/CaP nanoparticles with hydrothermal treatment was also studied by transmission electron microscopy (TEM), as shown in Fig. 2D. The spherical morphology and monodispersity of Gd-DTPA/CaP were confirmed from TEM images (Fig. 2D), and the size was calculated to be nearly 55 nm (Fig. 2E), which might correspond to the core size of Gd-DTPA/CaP as it is difficult to stain and detect their PEG layer by TEM. Moreover, no agglomeration of nanoparticles was observed from all of the TEM images, which may result from the efficient PEG surface decoration of the organic–inorganic hybrid structure prohibiting Gd-DTPA/CaP nanoparticles interact with each other, as we also confirmed that surface ξ-potential of Gd-DTPA/CaP was almost neutral (−0.5 mV). Therefore, hydrothermal treatment

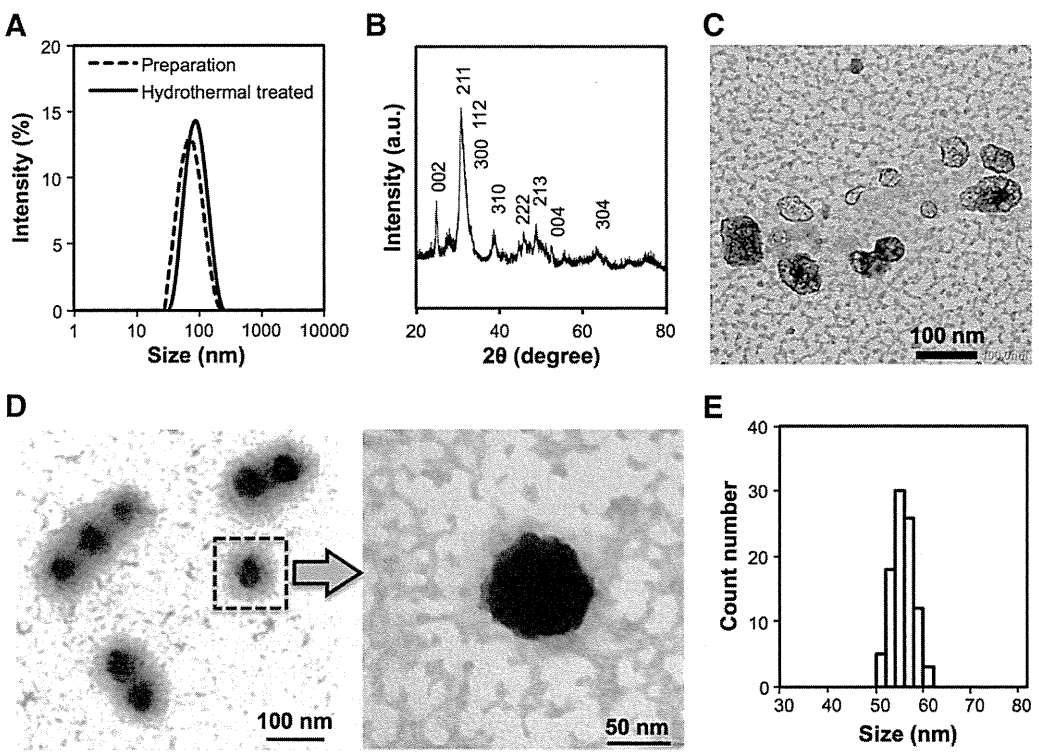

Fig. 2. Characteristics of Gd-DTPA/CaP nanoparticles. (A) DLS-measured z-average diameters of Gd-DTPA/CaP nanoparticles before and after hydrothermal treatment. (B) XRD pattern of Gd-DTPA/CaP nanoparticles, typical peaks of hydroxyapatite ($Ca_{10}(PO_4)_6(OH)_2$) were marked. (C) TEM image of purified Gd-DTPA/CaP nanoparticles without hydrothermal treatments. (D) TEM images of purified Gd-DTPA/CaP nanoparticles with hydrothermal treatments. (E) Number averaged size distribution of Gd-DTPA/CaP nanoparticles calculated from TEM images.

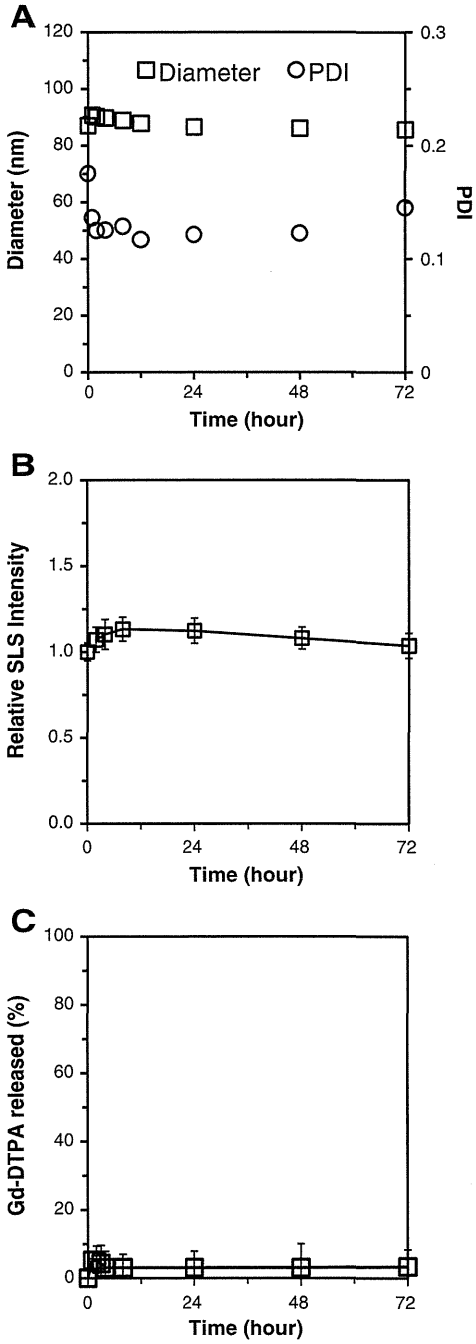

Fig. 3. *In vitro* characterization of Gd-DTPA/CaP nanoparticles in physiological conditions (10 mM PBS buffer, 140 mM NaCl, pH 7.4 and 37 °C). (A) Z-average diameter and PDI changes of Gd-DTPA/CaP determined by DLS. (B) Relative light scattering intensity changes of Gd-DTPA/CaP. (C) Release profiles of Gd-DTPA/CaP.

dramatically increased the stability of these organic–inorganic hybrid CaP nanoparticles in aqueous environments.

3.2. Colloidal stability and Gd-DTPA release profile of Gd-DTPA/CaP

To achieve specific and significant MR contrast enhancement at the tumor site *in vivo*, nanoparticles should be sufficiently stable during circulation in the bloodstream, while minimizing the leakage of contrast agents. Therefore, we evaluated the stability and Gd-DTPA release rate of Gd-DTPA/CaP nanoparticles under physiological conditions. Firstly, the stability of Gd-DTPA/CaP was studied by diluting in 10 mM PBS

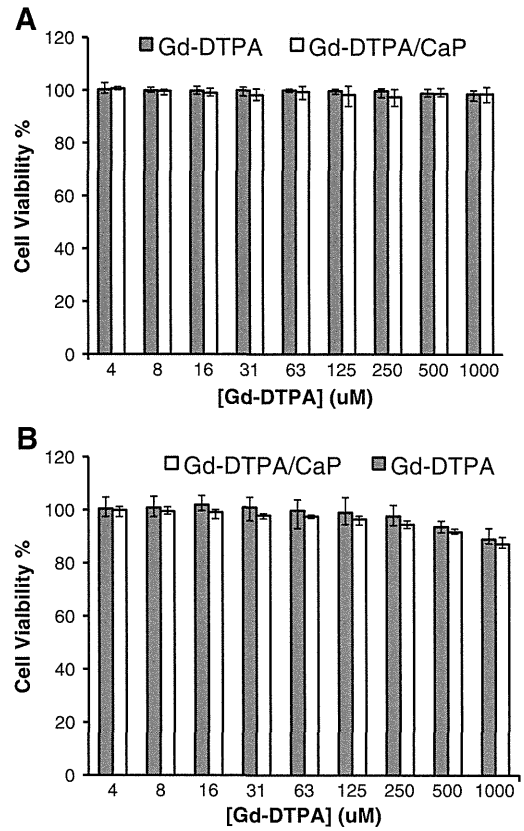

Fig. 4. Cytotoxicity results of Gd-DTPA/CaP against (A) C-26 cells and (B) HUVEC after 72 h incubation.

buffer (140 mM NaCl, pH 7.4) and incubated at 37 °C with continuous shaking. The Z-average diameter and PDI were determined by DLS, while the changes on the light scattering intensity were determined as they reflect the variation in the apparent molecule weight and concentration of nanoparticles. Accordingly, the z-average diameter and PDI of Gd-DTPA/CaP almost did not change at physiological condition (Fig. 3A). Besides, the relative light scattering intensity of Gd-DTPA/CaP nanoparticles increased a little in PBS buffer at initial 24 h and finally decreased slowly (Fig. 3B), this may be caused by interactions of Ca^{2+} with phosphate in PBS buffer. The DLS and SLS results demonstrated that hydrothermal treated Gd-DTPA/CaP nanoparticles were stable in physiological conditions. Moreover, the release profile of Gd-DTPA from Gd-DTPA/CaP in physiological conditions was obtained by measuring the amount of released Gd-DTPA by ICP-MS after dialysis against 10 mM PBS buffer (pH 7.4, NaCl 140 mM) at 37 °C. Thus, Gd-DTPA was slowly released from the nanoparticles, and only 5% of the loaded Gd-DTPA was released in 72 h (Fig. 3C), which was also contributed by the high stability of hydrothermal treated Gd-DTPA/CaP nanoparticles in physiological conditions.

3.3. Cytotoxicity of Gd-DTPA/CaP

The potential toxicity of nanoparticles is a dominant factor for their applications in clinical imaging. Moreover, rapid increase of intracellular Ca^{2+} over physiological concentration may induce cytotoxicity [32,54]. Therefore, we performed comparative dose–response cytotoxicity studies of Gd-DTPA/CaP and free Gd-DTPA against HUVEC and C-26 cells. After 72 h of exposure, no obvious cytotoxicity was found against both cell lines (Fig. 4). Herein, Gd-DTPA/CaP showed cell viability profiles similar to clinically approved Gd-DTPA, and the low cytotoxicity of Gd-DTPA/CaP benefits its further applications.

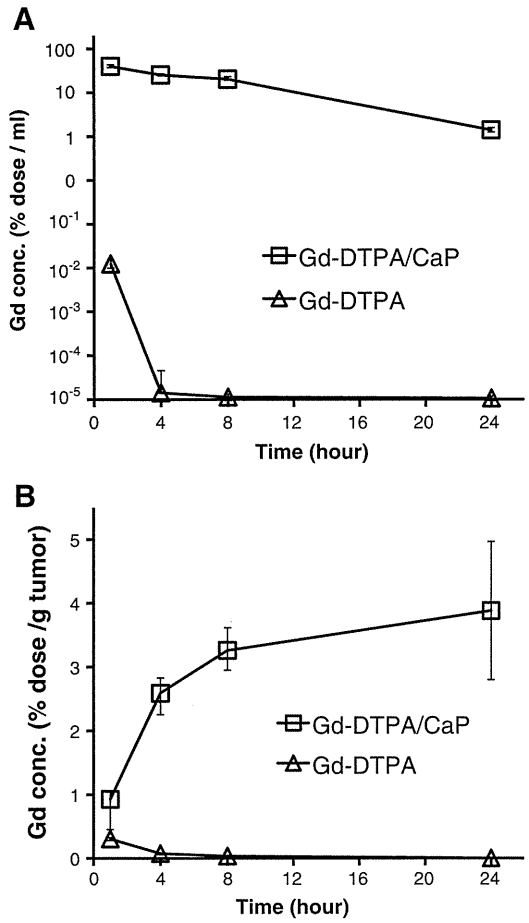

Fig. 5. *In vivo* biodistribution of Gd-DTPA/CaP and Gd-DTPA following tail-vein injection. (A) Log-linear blood circulation profiles of Gd-DTPA/CaP and Gd-DTPA. (B) Tumor accumulation levels of Gd-DTPA/CaP and Gd-DTPA.

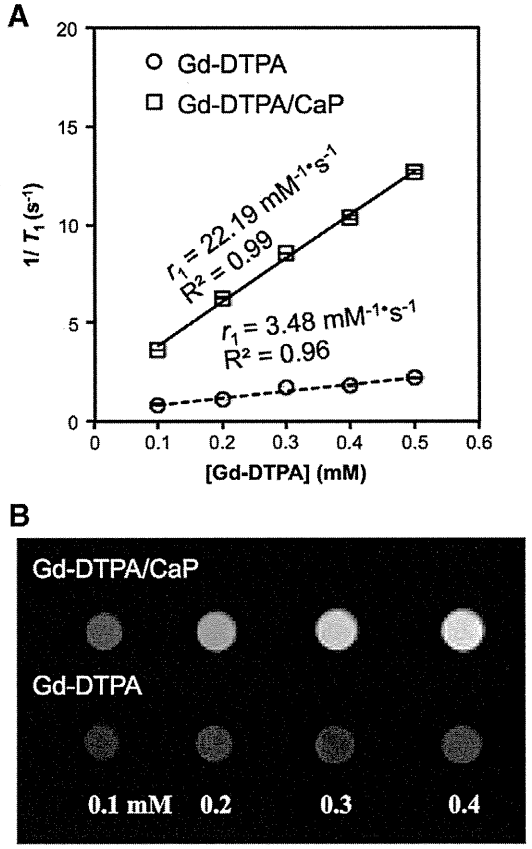

Fig. 7. MR enhancement effects of Gd-DTPA/CaP and Gd-DTPA. (A) T_1 relaxivity coefficients of Gd-DTPA/CaP and Gd-DTPA characterized by ^{1}H-NMR analyzer at 0.59 T. (B) T_1 weight MR images of Gd-DTPA/CaP and free Gd-DTPA solutions at 1 T MRI.

3.4. *In vivo* biodistribution of Gd-DTPA/CaP

Bioavailability and targeting ability of Gd-DTPA/CaP are extremely important for their *in vivo* applications, and can be reflected from plasma clearance and accumulation in tumors. Thus, we measured the amounts of Gd-DTPA delivered by Gd-DTPA/CaP in plasma and in subcutaneous C-26 tumors, and then compared the results with those after administration of free Gd-DTPA. Thus, free Gd-DTPA was rapidly cleared from plasma, and only trace amounts (nearly 0.001% dose/ml) were found in plasma 1 h after intravenous administration (Fig. 5A). Accordingly, Gd-DTPA is a small molecular compound, which could be

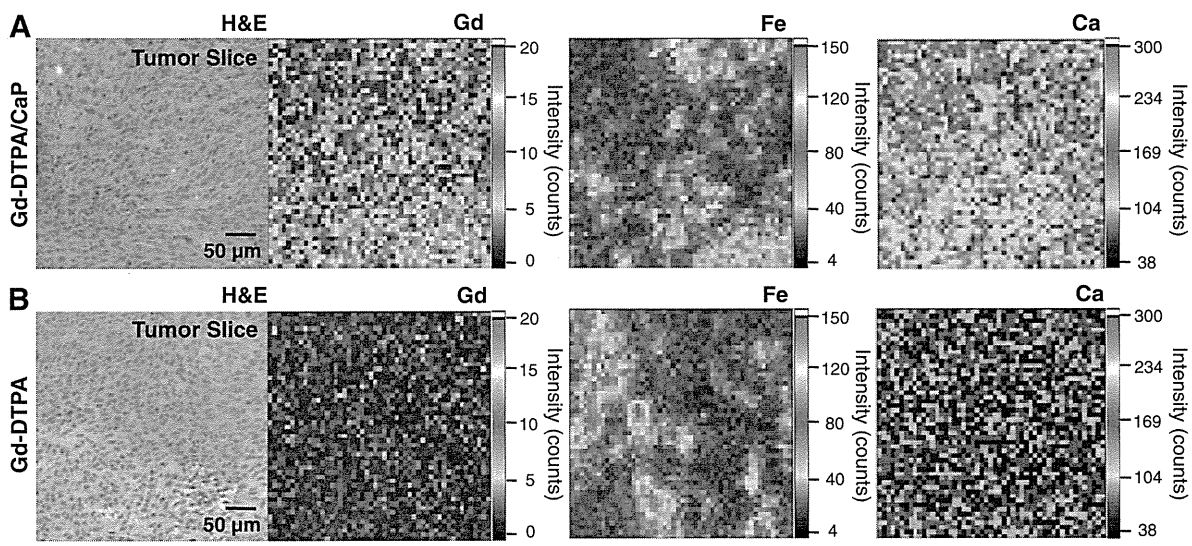

Fig. 6. Micro-distributions of Gd-DTPA/CaP and Gd-DTPA in tumor sections scanned by μ-SR-XRF. (A) H&E staining of tumor section and Gd, Fe and Ca elements distributions in tumor slice 4 h post intravenous injection of Gd-DTPA/CaP. (B) H&E staining of tumor section and Gd, Fe and Ca elements distributions in tumor slice 4 h post intravenous injection of Gd-DTPA.

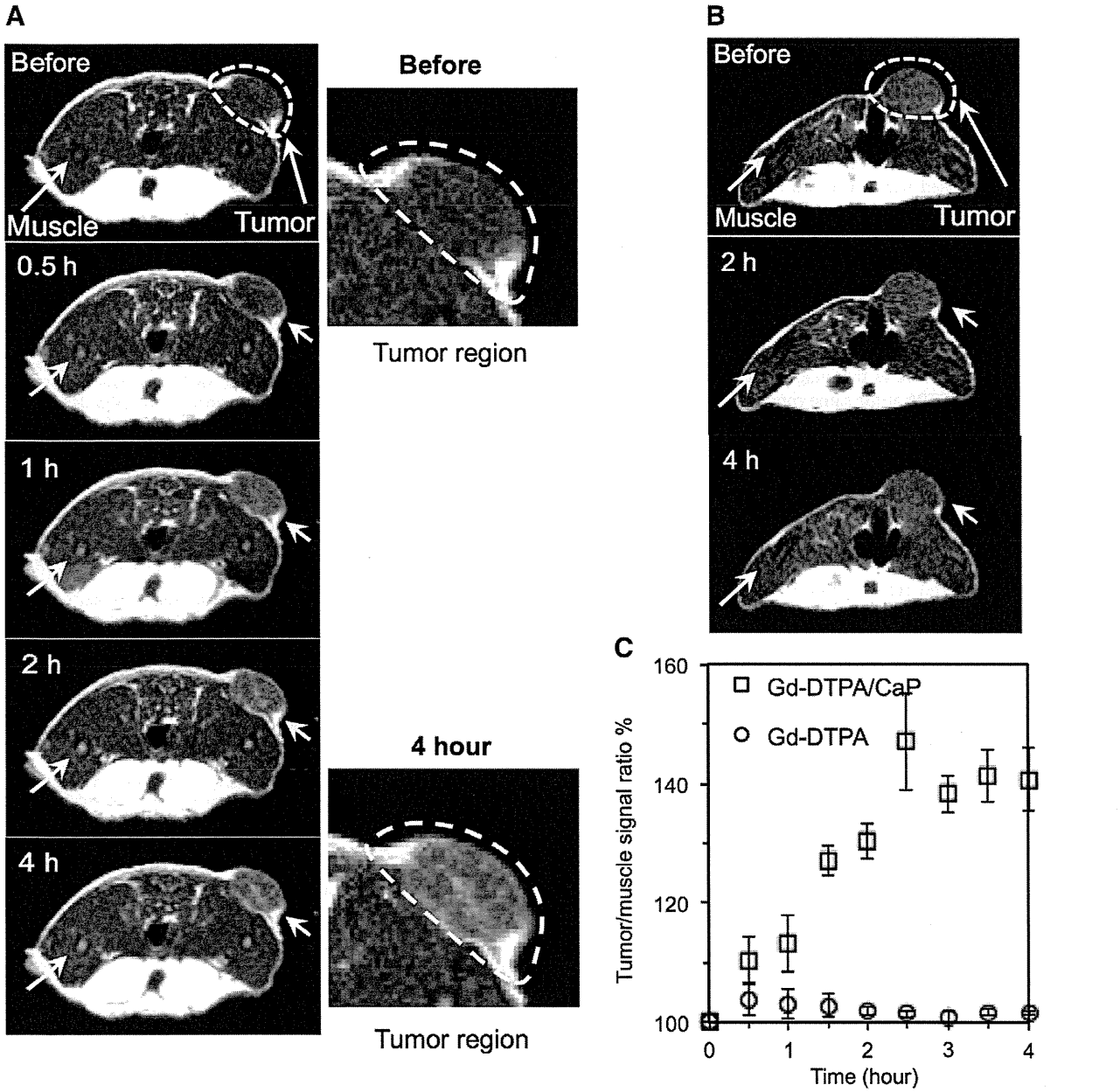

Fig. 8. *In vivo* MRI results of C-26 subcutaneous tumor model bearing Balb/c nude mice following tail-vein injection of Gd-DTPA/CaP and Gd-DTPA as contrast agents. (A) Represent MRI images of C-26 subcutaneous tumor model bearing Balb/c nude mice contrasted by Gd-DTPA/CaP after intravenous injection. (B) Represent MRI images of C-26 subcutaneous tumor model bearing Balb/c nude mice contrasted by Gd-DTPA after intravenous injection. (C) Tumor to muscle signal ratios calculated from MRI images.

easily excreted from blood circulation, and it has been reported that only 10% of injected Gd-DTPA remains in blood after 5 min of administration in rats [48]. Therefore, high doses or multi-injection of Gd (III) chelates is usually applied in clinical settings, but this may result in inaccuracies of diagnosis and potential toxicity [4]. Indeed, free Gd-DTPA did not accumulate in the tumor tissue (Fig. 5B). For Gd-DTPA/CaP, over 40% of Gd-DTPA was found in plasma 1 h after administration, and approximately 20% remained even 8 h later (Fig. 5A), indicating that the blood circulation time of Gd-DTPA was remarkably extended by loading in CaP nanoparticles. Gd-DTPA/CaP gradually accumulated in tumor positions after intravenous injection, to reach nearly 4% of the injected dose per gram tissue after 4 h (Fig. 5B). The accumulation profile may be contributed by the EPR effect observed for macromolecular drug carriers [24].

The extravasation and penetration of nanoparticles in tumors tissues critically affect their contrast enhancing ability, as they will determine the distribution and duration of the MR signal improvements [55]. Thus, we studied the micro-distribution of Gd-DTPA/CaP in the tumors by using micro-synchrotron radiation-induced X-ray fluorescence spectrometry (μ-SR-XRF). μ-SR-XRF is applied to analyze the element distribution of Gd and Ca from Gd-DTPA/CaP in tumor slices [51]. Moreover, Fe atoms from hemeproteins were detected to infer the presence of blood vessels. Accordingly, μ-SR-XRF was used to detect tumor slices harvested 4 h after administration of Gd-DTPA/CaP or free Gd-DTPA. As shown in Fig. 6, higher intensity of Ca and Gd was found in tumor slices administrated with Gd-DTPA/CaP than control Gd-DTPA, revealing the enhanced accumulation of Gd-DTPA/CaP. Moreover, the presence of the Gd and Ca atoms for Gd-DTPA/CaP was homogeneous and distant from the Fe-rich areas of blood vessels, suggesting deep tumor penetration of the Gd-DTPA/CaP nanoparticles.

3.5. MRI contrast enhancing ability of Gd-DTPA/CaP

For MRI probes, molecular relaxivity is an important parameter, which determines the contrast ability of a paramagnetic compound, as higher molecular relaxivity (r_1) contributes to higher signal enhancement. To evaluate the molecular relaxivity of Gd-DTPA loaded Gd-DTPA/CaP, we used a 0.59 T pulse-NMR. Thus, r_1 value of Gd-DTPA in Gd-DTPA/CaP increased nearly 6 times from 3.48 mM^{-1} s^{-1} of free Gd-DTPA to 22.19 mM^{-1} s^{-1} (Fig. 7A). The relaxivity of Gd^{3+} ions from $GdCl_3$ in aqueous solution was 10.61 mM^{-1} s^{-1}, which is lower than Gd-DTPA/CaP. Meanwhile, the r_1 of Gd-DTPA released from Gd-DTPA/CaP by dialysis of Gd-DTPA/CaP in Mili-Q water was 3.34 mM^{-1} s^{-1} (Fig. S1), which is similar to that of Gd-DTPA, suggesting there was no free Gd^{3+} ion in Gd-DTPA/CaP nanoparticles. In addition, 1 T MRI results confirmed that Gd-DTPA/CaP has higher contrast ability than Gd-DTPA, as the images of Gd-DTPA/CaP were much whiter than free Gd-DTPA at the same concentration (Fig. 7B). The high molecular relaxivity of Gd-DTPA/CaP may result from both the additive effect of all of the Gd^{3+} paramagnetic centers and the reduction of molecular tumbling rates, which increases the r_1 value of each Gd-chelate in the confined space of CaP [17–19,21,26].

Finally, Gd-DTPA/CaP and Gd-DTPA were used to enhance the MR contrast of C-26 subcutaneous tumors *in vivo* (Fig. 8A and B). After intravenous injection of Gd-DTPA/CaP, the contrast of the tumor position was gradually enhanced, reaching more than 40% increase in the signal ratio of the tumor to the muscle at 4 h-post administration (Fig. 8C). The higher contrast of tumor positions by Gd-DTPA/CaP might result from both the promoted accumulation of Gd-DTPA and the increased molecular relaxivity of Gd-DTPA inside Gd-DTPA/CaP. By incorporation of Gd-DTPA inside sub-100 nm CaP nanoparticles, higher amounts of contrast agent were selectively delivered to tumor positions by EPR effect (Fig. 5), increasing the contrast with the surrounding tissues. Meanwhile, as Gd-DTPA/CaP exhibited higher molecular relaxivity than free Gd-DTPA, the contrast in tumor positions was enhanced more efficiently than the conventional contrast agent. Thus, no signal enhancement was observed for free Gd-DTPA even administrated with 4 times higher dose than that of Gd-DTPA/CaP. These results demonstrated that MRI contrast enhancing ability of Gd-DTPA was greatly improved by incorporation into CaP nanoparticles.

4. Conclusion

In this study, Gd-DTPA/CaP nanoparticles with unique colloidal stability, biodegradation and magnetic properties were synthesized by following a facile two-step preparation approach, and used for MRI contrast enhancement of solid tumors. Thus, as all of the components are non-toxic and biocompatible materials, Gd-DTPA/CaP is expected to become an important candidate for diagnosis of malignant tumors. Moreover, the two-step preparation method of Gd-DTPA/CaP represents a facile and promising strategy for incorporating bioactive molecules in CaP nanoparticles for the construction of safe and efficient drug carriers for biomedical applications. The hydrothermal treatment procedure significantly enhanced the colloidal stability of CaP nanoparticles and the relaxivity of Gd-DTPA was enhanced after loading in the CaP matrix. This strategy may be utilized to develop other CaP-based drug delivery systems, and further applied for developing other inorganic-materials based nanocarriers.

Acknowledgments

This research was financially supported by Funding Program for World-Leading Innovative R&D on Science and Technology (FIRST) from the Japan Society for the Promotion of Science (JSPS) (K.K.) and Takeda Science Foundation (N.N.). P.M. thanks the support of a JSPS fellowship. TEM measurements were conducted in Research Hub for Advanced Nano Characterization, The University of Tokyo, supported by the Ministry of Education, Culture, Sports, Science and Technology (MEXT), Japan. μ-SR-XRF characterizations were supported by the Nanotechnology Support Program of the Japan Synchrotron Radiation Research Institute (JASRI). We thank Ms. Sayaka Shibata and Ms. Aiko Sekita (NIRS) for technical support.

Appendix A. Supplementary data

Supplementary data to this article can be found online at http://dx.doi.org/10.1016/j.jconrel.2013.10.038.

References

[1] M.G. Harisinghani, J. Barentsz, P.F. Hahn, W.M. Deserno, S. Tabatabaei, C.H. van de Kaa, J. de la Rosette, R. Weissleder, Noninvasive detection of clinically occult lymph-node metastases in prostate cancer, N. Engl. J. Med. 348 (2003) 2491–2499.
[2] H.B. Na, T. Hyeon, Nanostructured T1 MRI contrast agents, J. Mater. Chem. 19 (2009) 6267–6273.
[3] P. Caravan, J.J. Ellison, T.J. McMurry, R.B. Lauffer, Gadolinium (III) chelates as MRI contrast agents: structure, dynamics, and applications, Chem. Rev. 99 (1999) 2293–2352.
[4] M.F. Kircher, A. de la Zerda, J.V. Jokerst, C.L. Zavaleta, P.J. Kempen, E. Mittra, K. Pitter, R.M. Huang, C. Campos, F. Habte, R. Sinclair, C.W. Brennan, I.K. Mellinghoff, E.C. Holland, S.S. Gambhir, A brain tumor molecular imaging strategy using a new triple-modality MRI-photoacoustic-raman nanoparticle, Nat. Med. 18 (2012) 829–834.
[5] N. Nasongkla, E. Bey, J.M. Ren, H. Ai, C. Khemtong, J.S. Guthi, S.F. Chin, A.D. Sherry, D.A. Boothman, J.M. Gao, Multifunctional polymeric micelles as cancer-targeted, MRI-ultrasensitive drug delivery systems, Nano Lett. 6 (2006) 2427–2430.
[6] P. Mi, H. Cabral, D. Kokuryo, M. Rafi, Y. Terada, I. Aoki, T. Saga, T. Ishii, N. Nishiyama, K. Kataoka, Gd-DTPA-loaded polymer-metal complex micelles with high relaxivity for MR cancer imaging, Biomaterials 34 (2013) 492–500.
[7] S. Kaida, H. Cabral, M. Kumagai, A. Kishimura, Y. Terada, M. Sekino, I. Aoki, N. Nishiyama, T. Tani, K. Kataoka, Visible drug delivery by supramolecular nanocarriers directing to single-platformed diagnosis and therapy of pancreatic tumor model, Cancer Res. 70 (2010) 7031–7041.
[8] J. Lu, S.L. Ma, J.Y. Sun, C.C. Xia, C. Liu, Z.Y. Wang, X.N. Zhao, F.B. Gao, Q.Y. Gong, B. Song, X.T. Shuai, H. Ai, Z.W. Gu, Manganese ferrite nanoparticle micellar nanocomposites as MRI contrast agent for liver imaging, Biomaterials 30 (2009) 2919–2928.
[9] H. Ai, C. Flask, B. Weinberg, X. Shuai, M.D. Pagel, D. Farrell, J. Duerk, J.M. Gao, Magnetite-loaded polymeric micelles as ultrasensitive magnetic-resonance probes, Adv. Mater. 17 (2005) 1949–1952.
[10] E. Nakamura, K. Makino, T. Okano, T. Yamamoto, M. Yokoyama, A polymeric micelle MRI contrast agent with changeable relaxivity, J. Control. Release 114 (2006) 325–333.
[11] G. Mikhaylov, U. Mikac, A.A. Magaeva, V.I. Itin, E.P. Naiden, I. Psakhye, L. Babes, T. Reinheckel, C. Peters, R. Zeiser, M. Bogyo, V. Turk, S.G. Psakhye, B. Turk, O. Vasiljeva, Ferri-liposomes as an MRI-visible drug-delivery system for targeting tumours and their microenvironment, Nat. Nanotechnol. 6 (2011) 594–602.
[12] Z.Y. Liao, H.J. Wang, X.D. Wang, P.Q. Zhao, S. Wang, W.Y. Su, J. Chang, Multifunctional nanoparticles composed of a poly(DL-lactide-coglycolide) core and a paramagnetic liposome shell for simultaneous magnetic resonance imaging and targeted therapeutics, Adv. Funct. Mater. 21 (2011) 1179–1186.
[13] H. Grull, S. Langereis, L. Messager, D.D. Castelli, A. Sanino, E. Torres, E. Terreno, S. Aime, Block copolymer vesicles containing paramagnetic lanthanide complexes: a novel class of T-1- and CEST MRI contrast agents, Soft Matter 6 (2010) 4847–4850.
[14] D. Kokuryo, Y. Anraku, A. Kishimura, S. Tanaka, M.R. Kano, J. Kershaw, N. Nishiyama, T. Saga, I. Aoki, K. Kataoka, SPIO-PICsome: development of a highly sensitive and stealth-capable MRI nano-agent for tumor detection using SPIO-loaded unilamellar polyion complex vesicles (PICsomes), J. Control. Release 169 (2013) 220–227.
[15] H.Y. Lee, Z. Li, K. Chen, A.R. Hsu, C.J. Xu, J. Xie, S.H. Sun, X.Y. Chen, PET/MRI dual-modality tumor imaging using arginine-glycine-aspartic (RGD)-conjugated radiolabeled iron oxide nanoparticles, J. Nucl. Med. 49 (2008) 1371–1379.
[16] M. Kumagai, M.R. Kano, Y. Morishita, M. Ota, Y. Imai, N. Nishiyama, M. Sekino, S. Ueno, K. Miyazono, K. Kataoka, Enhanced magnetic resonance imaging of experimental pancreatic tumor *in vivo* by block copolymer-coated magnetite nanoparticles with TGF-beta inhibitor, J. Control. Release 140 (2009) 306–311.
[17] E. Vucic, H.M. Sanders, F. Arena, E. Terreno, S. Aime, K. Nicolay, E. Leupold, M. Dathe, N.A. Sommerdijk, Z.A. Fayad, W.J.M. Mulder, Well-defined, multifunctional nanostructures of a paramagnetic lipid and a lipopeptide for macrophage imaging, J. Am. Chem. Soc. 131 (2009) 406–407.
[18] W.J.M. Mulder, G.J. Strijkers, G.A.F. van Tilborg, A.W. Griffioen, K. Nicolay, Lipid-based nanoparticles for contrast-enhanced MRI and molecular imaging, NMR Biomed. 19 (2006) 142–164.
[19] F. Kielar, L. Tei, E. Terreno, M. Botta, Large relaxivity enhancement of paramagnetic lipid nanoparticles by restricting the local motions of the Gd-III chelates, J. Am. Chem. Soc. 132 (2010) 7836–7837.
[20] G.L. Liang, J. Ronald, Y.X. Chen, D.J. Ye, P. Pandit, M.L. Ma, B. Rutt, J.H. Rao, Controlled self-assembling of gadolinium nanoparticles as smart molecular magnetic resonance imaging contrast agents, Angew. Chem. Int. Ed. 50 (2011) 6283–6286.

[21] A.K. Duncan, P.J. Klemm, K.N. Raymond, C.C. Landry, Silica microparticles as a solid support for gadolinium phosphonate magnetic resonance imaging contrast agents, J. Am. Chem. Soc. 134 (2012) 8046–8049.
[22] M.F. Bennewitz, T.L. Lobo, M.K. Nkansah, G. Ulas, G.W. Brudvig, E.M. Shapiro, Biocompatible and pH-sensitive PLGA encapsulated MnO nanocrystals for molecular and cellular MRI, ACS Nano 5 (2011) 3438–3446.
[23] L.M. Manus, D.J. Mastarone, E.A. Waters, X.Q. Zhang, E.A. Schultz-Sikma, K.W. MacRenaris, D. Ho, T.J. Meade, Gd(III)-nanodiamond conjugates for MRI contrast enhancement, Nano Lett. 10 (2010) 484–489.
[24] Y. Matsumura, H. Maeda, A new concept for macromolecular therapeutics in cancer chemotherapy: mechanism of tumoritropic accumulation of proteins and the antitumor agent smancs, Cancer Res. 46 (1986) 6387–6392.
[25] P. Caravan, C.T. Farrar, L. Frullano, R. Uppal, Influence of molecular parameters and increasing magnetic field strength on relaxivity of gadolinium- and manganese-based T_1 contrast agents, Contrast Media Mol. Imaging 4 (2009) 89–100.
[26] J.S. Ananta, B. Godin, R. Sethi, L. Moriggi, X.W. Liu, R.E. Serda, R. Krishnamurthy, R. Muthupillai, R.D. Bolskar, L. Helm, M. Ferrari, L.J. Wilson, P. Decuzzi, Geometrical confinement of gadolinium-based contrast agents in nanoporous particles enhances T_1 contrast, Nat. Nanotechnol. 5 (2010) 815–821.
[27] M. Liong, J. Lu, M. Kovochich, T. Xia, S.G. Ruehm, A.E. Nel, F. Tamanoi, J.I. Zink, Multifunctional inorganic nanoparticles for imaging, targeting, and drug delivery, ACS Nano 2 (2008) 889–896.
[28] H. Cabral, N. Nishiyama, K. Kataoka, Supramolecular nanodevices: from design validation to theranostic nanomedicine, Acc. Chem. Res. 44 (2011) 999–1008.
[29] A. Jemal, F. Bray, M.M. Center, J. Ferlay, E. Ward, D. Forman, Global cancer statistics, CA Cancer J. Clin. 61 (2011) 69–90.
[30] F.L. Graham, A.J. van der Eb, A new technique for the assay of infectivity of human adenovirus 5 DNA, Virology 52 (1973) 456–467.
[31] M. Epple, K. Ganesan, R. Heumann, J. Klesing, A. Kovtun, S. Neumann, V. Sokolova, Application of calcium phosphate nanoparticles in biomedicine, J. Mater. Chem. 20 (2010) 18–23.
[32] A. Tabakovic, M. Kester, J.H. Adair, Calcium phosphate-based composite nanoparticles in bioimaging and therapeutic delivery applications, Wiley Interdiscip. Rev. Nanomedicine Nanobiotechnol 4 (2012) 96–112.
[33] M.Z. Zhang, K. Kataoka, Nano-structured composites based on calcium phosphate for cellular delivery of therapeutic and diagnostic agents, Nano Today 4 (2009) 508–517.
[34] R.Z. LeGeros, Biodegradation and bioresorption of calcium phosphate ceramics, Clin. Mater. 14 (1993) 65–88.
[35] E.I. Altinoglu, T.J. Russin, J.M. Kaiser, B.M. Barth, P.C. Eklund, M. Kester, J.H. Adair, Near-infrared emitting fluorophore-doped calcium phosphate nanoparticles for in vivo imaging of human breast cancer, ACS Nano 2 (2008) 2075–2084.
[36] J. Li, Y.C. Chen, Y.C. Tseng, S. Mozumdar, L. Huang, Biodegradable calcium phosphate nanoparticle with lipid coating for systemic siRNA delivery, J. Control. Release 142 (2010) 416–421.
[37] V.V. Sokolova, I. Radtke, R. Heumann, M. Epple, Effective transfection of cells with multi-shell calcium phosphate-DNA nanoparticles, Biomaterials 27 (2006) 3147–3153.
[38] V.V. Sokolova, T. Knuschke, A. Kovtun, J. Buer, M. Epple, A.M. Westendorf, The use of calcium phosphate nanoparticles encapsulating toll-like receptor ligands and the antigen hemagglutinin to induce dendritic cell maturation and T cell activation, Biomaterials 31 (2010) 5627–5633.
[39] A.H. Faraji, P. Wipf, Nanoparticles in cellular drug delivery, Bioorg. Med. Chem. 17 (2009) 2950–2962.
[40] G.K. Lim, J. Wang, S.C. Ng, L.M. Gan, Formation of nanocrystalline hydroxyapatite in nonionic surfactant emulsions, Langmuir 15 (1999) 7472–7477.
[41] Y. Kakizawa, K. Kataoka, Block copolymer self-assembly into monodispersive nanoparticles with hybrid core of antisense DNA and calcium phosphate, Langmuir 18 (2002) 4539–4543.
[42] F. Pittella, M.Z. Zhang, Y. Lee, H.J. Kim, T. Tockary, K. Osada, T. Ishii, K. Miyata, N. Nishiyama, K. Kataoka, Enhanced endosomal escape of siRNA-incorporating hybrid nanoparticles from calcium phosphate and PEG-block charge-conversional polymer for efficient gene knockdown with negligible cytotoxicity, Biomaterials 32 (2011) 3106–3114.
[43] Y. Kakizawa, K. Miyata, S. Furukawa, K. Kataoka, Size-controlled formation of a calcium phosphate-based organic–inorganic hybrid vector for gene delivery using poly(ethylene glycol)-*block*-poly(aspartic acid), Adv. Mater. 16 (2004) 699–702.
[44] Y. Kakizawa, S. Furukawa, A. Ishii, K. Kataoka, Organic–inorganic hybrid-nanocarrier of siRNA constructing through the self-assembly of calcium phosphate and PEG-based block aniomer, J. Control. Release 111 (2006) 368–370.
[45] Y. Kakizawa, S. Furukawa, K. Kataoka, Block copolymer-coated calcium phosphate nanoparticles sensing intracellular environment for oligodeoxynucleotide and siRNA delivery, J. Control. Release 97 (2004) 345–356.
[46] F. Pittella, K. Miyata, Y. Maeda, T. Suma, S. Watanabe, Q. Chen, R.J. Christie, K. Osada, N. Nishiyama, K. Kataoka, Pancreatic cancer therapy by systemic administration of VEGF siRNA contained in calcium phosphate/charge-conversional polymer hybrid nanoparticles, J. Control. Release 161 (2012) 868–874.
[47] M. Zhang, A. Ishii, N. Nishiyama, S. Matsumoto, T. Ishii, Y. Yamasaki, K. Kataoka, PEGylated calcium phosphate nanocomposites as smart environment-sensitive carriers for siRNA delivery, Adv. Mater. 21 (2009) 1–6.
[48] H.J. Weinmann, R.C. Brasch, W.R. Press, G.E. Wesbey, Characteristics of gadolinium-DTPA complex: a potential NMR contrast agent, AJR Am. J. Roentgenol. 142 (1984) 619–624.
[49] Y.J. Wang, S.H. Zhang, K. Wei, N.R. Zhao, J.D. Chen, X.D. Wang, Hydrothermal synthesis of hydroxyapatite nanopowders using cationic surfactant as a template, Mater. Lett. 60 (2006) 1484–1487.
[50] A. Koide, A. Kishimura, K. Osada, W.D. Jang, Y. Yamasaki, K. Kataoka, Semipermeable polymer vesicle (PICsome) self-assembled in aqueous medium from a pair of oppositely charged block copolymers: physiologically stable micro-/nanocontainers of water-soluble macromolecules, J. Am. Chem. Soc. 128 (2006) 5988–5989.
[51] Y. Terada, S. Goto, N. Takimoto, K. Takeshita, H. Yamazaki, Y. Shimizu, S. Takahashi, H. Ohashi, Y. Furukawa, T. Matsushita, T. Ohata, Y. Ishizawa, T. Uruga, H. Kitamura, T. Ishikawa, S. Hayakawa, Construction and commissioning of BL37XU at SPring-8, AIP Conf. Proc. 705 (2004) 376–379.
[52] L. Yan, Y.D. Li, Z.X. Deng, J. Zhuang, X.M. Sun, Surfactant-assisted hydrothermal synthesis of hydroxyapatite nanorods, Int. J. Inorg. Mater. 3 (2001) 633–637.
[53] A.A. Chaudhry, S. Haque, S. Kellici, P. Boldrin, I. Rehman, A.K. Fazal, J.A. Darr, Instant nano-hydroxyapatite: a continuous and rapid hydrothermal synthesis, Chem. Commun. 21 (2006) 2286–2288.
[54] C. Cerella, M. Diederich, L. Ghibelli, The dual role of calcium as messenger and stressor in cell damage, death, and survival, Int. J. Cell Biol. 2010 (2010) 1–14.
[55] A.I. Minchinton, I.F. Tannock, Drug penetration in solid tumours, Nat. Rev. Cancer 6 (2006) 583–592.

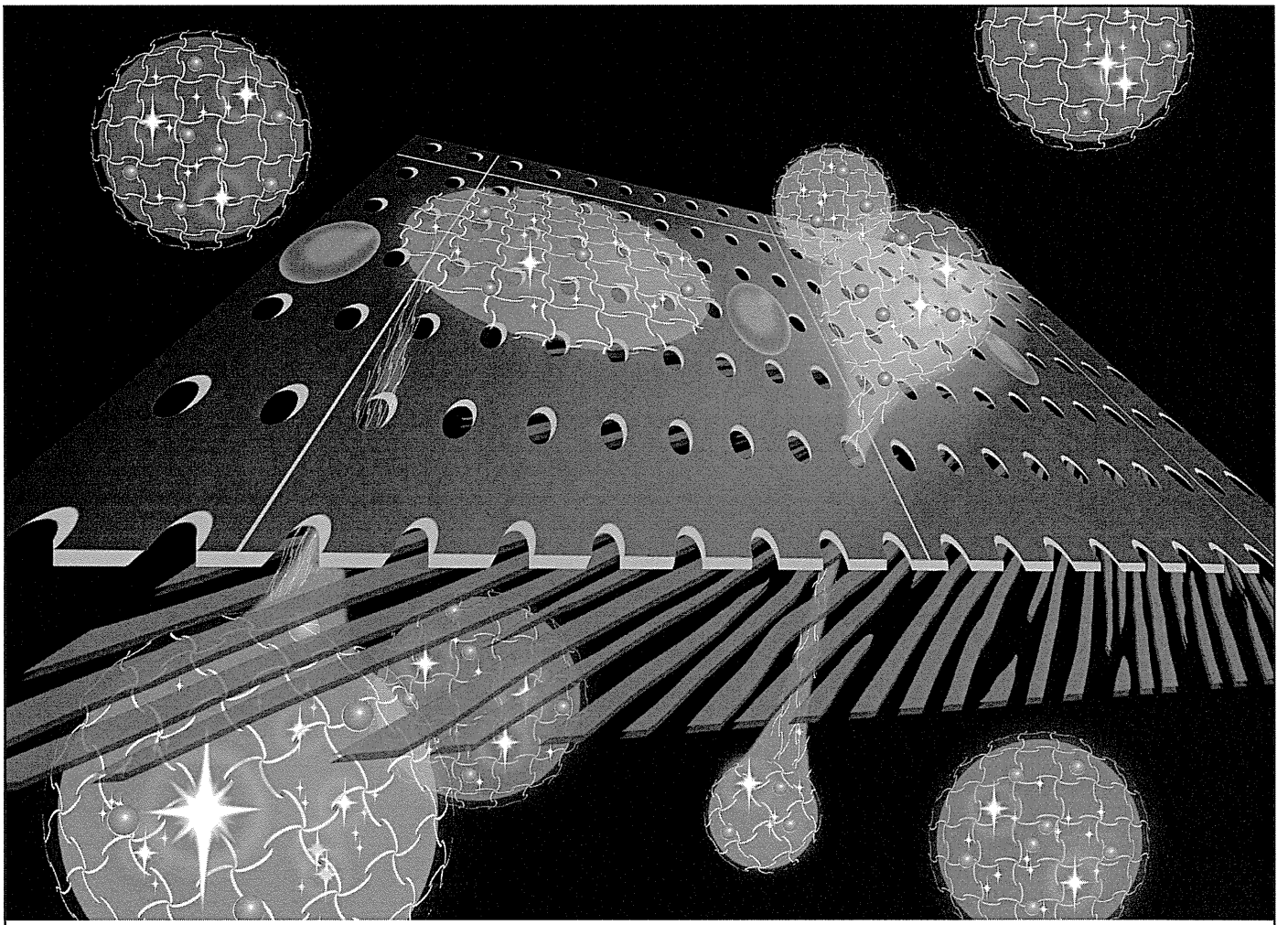

Showcasing collaborative research from the Masaru Kato lab (Graduate School of Pharmaceutical Sciences and GPLLI Program, The University of Tokyo, Tokyo, Japan), and the Ichio Aoki lab (Molecular Imaging Center, National Institute of Radiological Sciences, Chiba, Japan).

Title: The simple preparation of polyethylene glycol-based soft nanoparticles containing dual imaging probes

The PEG-based nanoparticles that encapsulate dual imaging probes were soft and excreted by the mice rapidly through urine. The PEG-based soft nanoparticles will be a safer carrier for diagnostic agents.

As featured in:

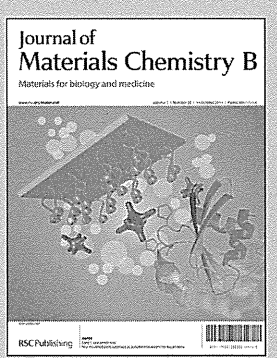

See S. Murayama *et al.*, *J. Mater. Chem. B*, 2013, **1**, 4932.

RSC Publishing

www.rsc.org/MaterialsB

Registered Charity Number 207890

Journal of Materials Chemistry B

RSC Publishing

PAPER

View Article Online
View Journal | View Issue

The simple preparation of polyethylene glycol-based soft nanoparticles containing dual imaging probes†

Cite this: J. Mater. Chem. B, 2013, 1, 4932

Shuhei Murayama,[ab] Jun-ichiro Jo,[b] Yuka Shibata,[a] Kun Liang,[c] Tomofumi Santa,[a] Tsuneo Saga,[b] Ichio Aoki[b] and Masaru Kato*[a]

Received 10th June 2013
Accepted 30th July 2013

DOI: 10.1039/c3tb20828a

www.rsc.org/MaterialsB

We developed a simple method to prepare PEG-based soft nanoparticles that encapsulate dual imaging probes. Because the probes could be encapsulated by either chemical or physical means, a variety of probe molecules were encapsulated within the nanoparticles simultaneously. The nanoparticles were administrated to mice and the pharmacokinetics of the nanoparticles was analyzed by means of MRI, fluorescence spectroscopy, and transmission electron microscopy. The soft nanoparticles were excreted by the mice rapidly through the urine without collapse of the nanoparticles and without leaking of the probe molecules, and no accumulation of the nanoparticles in the body was observed. The pharmacokinetics of the nanoparticles was not changed by the encapsulated molecules and acute toxicity to mice was negligible. It was expect that these PEG-based soft nanoparticles will be applicable for use as a safe diagnostic agent.

Introduction

Dual or multi-probe molecules, which are composed of combinations of two or more functional molecules, are attractive for use as tools for noninvasive diagnosis and therapy.[1–4] Such dual and multi-probes improve the reliability and safety of the diagnoses as they mutually complement one another.

Although many dual or multi-probes have been reported, most of these probes have been designed by bonding two different probe molecules directly or indirectly with the aid of a linker molecule.[1–6] For the linkage of two different probe molecules, the probe molecules must have appropriate functional groups for linkages and must also retain their functionality after being linked. Nanoparticles are promising materials for dual or multi-probe preparation because in addition to bonding, encapsulation and adsorption they are available for the immobilization of probe molecules to the nanoparticles.[7–12] In general, small nanoparticles show low potential toxicity risk, because they are rapidly excreted through the urine and they are suitable for clinical applications. However, the sensitivity of them is low, because of their small volume. For this reason, large nanoparticles that are excreted through the urine are ideal materials in terms of safety and detection.

We have developed a method for preparing polyethylene glycol (PEG)-based nanoparticles that contain various kinds of probe molecules, as reported previously.[13,14] The nanoparticles were prepared from monomer molecules that consisted of four long PEG chains with acryloyl groups at each chain end. Simply adding the probe molecules to a solution of the monomers resulted in the formation of uniformly sized nanoparticles that encapsulated the probe molecules. Because the encapsulated molecules are physically trapped by the mesh structure of the nanoparticles and because no chemical bonding between the molecules and PEG is required for encapsulation,[15,16] we concluded that there are no limitations to the types of molecules that can be encapsulated using this technique. Only two acryloyl groups were required to form a mesh structure for physical encapsulation of molecules within the nanoparticles, and thus we expected that the one of the two remaining acryloyl groups on each monomer could be used for chemical reactions with the probe molecules. To test this hypothesis, we encapsulated probe molecules in the PEG-based nanoparticles, by chemical means, in addition to the physical encapsulation. We speculated that if we encapsulated two different probes using two different (*i.e.*, chemical and physical) methods simultaneously, a dual probe could be prepared without limitation of the encapsulated molecules. In this study, we prepared three different dual probe nanoparticles containing physically and chemically encapsulated probe molecules. The physical properties of these nanoparticles were examined, and the nanoparticles were used for animal experiments to examine their pharmacokinetics and toxicity.

[a]*Graduate School of Pharmaceutical Sciences and GPLLI Program The University of Tokyo, 7-3-1 Hongo, Bunkyo-ku, Tokyo 113-0033, Japan. E-mail: masaru-kato@umin.ac.jp*

[b]*Molecular Imaging Center, National Institute of Radiological Sciences, 4-9-1 Anagawa, Inage-ku, Chiba 263-8555, Japan*

[c]*Center for Medical Systems Innovation Summer Internship Program, The University of Tokyo, Japan*

† Electronic supplementary information (ESI) available. See DOI: 10.1039/c3tb20828a

Experimental section

Materials

Tetra-poly(ethyl glycol)-amine (SUNBRIGHT PTE-050PA; M_n, 5328 g mol^{-1}) was purchased from NOF Corporation (Tokyo, Japan). *N*,*N*,*N*′,*N*′-Tetramethylethylenediamine (TEMED), triethylamine (TEA), acryloyl chloride (AC), dichloromethane (DCM), ammonium persulfate (APS), tris(hydroxymethyl) aminomethane (Tris), hydrochloric acid, methanol, diethyl ether, acetic acid, magnesium sulfate, fluorescein (Flu), and 4-(4,6-dimethoxy-1,3,5-triazin-2-yl)-4-methylmorpholinium chloride *n*-hydrate (DMT-MM) were purchased from Wako Pure Chemical Industries (Osaka, Japan). Dextran with a weight-averaged molecular weight of 40 000 (Dex), diethylenetriaminepentaacetic acid (DTPA) anhydride, manganese chloride, ferritin type I from horse spleen, and fluorescein isothiocyanate–dextran, molecular weight of 40 000 (Dex–Flu) was purchased from Sigma-Aldrich (St. Louis, MO). Alexa Fluor 647 carboxylic acid, succinimidyl ester was purchased from Invitrogen Corporation (Carlsbad, CA). Dimethyl sulfoxide (DMSO), 2-morpholineoethanesulfonic acid and 4-dimethylaminopyridine (DMAP) were obtained from Nacalai Tesque. Inc. (Kyoto, Japan). 2-Hydroxyethyl acrylate (AC-OH) was purchased from Tokyo Chemical Industry Co., LTD. (Tokyo, Japan). Water was purified with a Milli-Q apparatus (Millipore, Bedford, MA).

Preparation of Dex-Mn

DTPA anhydride (920 μmol) and DMAP (130 μmol) were added to 10 mL of dehydrated dimethyl sulfoxide containing 100 mg (1.9 mmol of hydroxyl (OH) groups) of dextran. The reaction solution was agitated at room temperature for 18 h to introduce DTPA residues to the OH of dextran, followed by dialysis against double distilled water for 2 days and freeze-drying to obtain DTPA-introduced dextran (Dex-DTPA). The extent of DTPA residues introduced to dextran OH groups was measured by conventional conductometric titration and calculated to be 10.2%. To 1 mL of Dex-DTPA solution (10 mg mL^{-1}, 19 μmol DTPA), 0.2 mL of manganese chloride solution (94 mg mL^{-1}, 95 μmol) was added in 0.1 M 2-morpholineoethanesulfate (MES)-buffered solution (pH 6.0). The mixtures were agitated at room temperature for 3 h to chelate Mn^{2+} to the DTPA residues. The reaction solution was purified by a PD-10 column (GE healthcare UK Ltd., Buckinghamshire, UK) with water and freeze-drying to obtain Mn^{2+}-chelated Dex-DTPA (Dex-Mn). The extent of Mn^{2+} chelated to DTPA residues was measured by atomic absorption spectrophotometer (AA-6800, Shimadzu Corp., Kyoto, Japan) and calculated to be 75%.

Preparation of short wave fluorescence linker (PEG-Flu-3AC)

Tetra-poly(ethyl glycol)-amine (**2**) (120 μmol) and Flu (**1**) (120 μmol) were dissolved in methanol and stirred until all reactants were dissolved in a lightproof vial. After that, DMT-MM (300 μmol) was added to start the synthesis without stirring. The reaction was done at room temperature for 3 h. The product was precipitated in diethyl ether on ice and filtered. The collected substance was washed with diethyl ether and dissolved in water. The aqueous solution was evaporated, dialyzed (SpectraPor6, CO 1000 g mol^{-1}) and freeze-dried to yield a fluorescent product (PEG-Flu-3NH (**3**)). PEG-Flu-3NH (18 μmol) was dissolved in dry DCM and stirred in a lightproof vial purged with N_2 gas. TEA (71 μmol) and excess amount of AC (177 μmol) were added dropwise on ice and stirred 3 h. After the reaction, the product was resolved in methanol, precipitated in diethyl ether on ice and filtered. The collected substance was washed with diethyl ether and dissolved in water. The aqueous solution was evaporated, dialyzed (SpectraPor6, CO 1000 g mol^{-1}) and freeze-dried to yield a fluorescent product (PEG-Flu-3AC (**4**)) (Scheme 1).

Preparation of the long wave fluorescence linker (Alexa-AC)

An excess amount of AC-OH (**5**) (666 μmol) and DMAP (66 μmol) were dissolved in DCM and stirred in a lightproof vial purged with N_2 gas. Then, Alexa Fluor 647 carboxylic acid (**6**), succinimidyl ester (1 μmol) in DMSO was added dropwise, and the mixture was stirred for 32 h at room temperature. After the reaction, the product was neutralized by adding diluted acetic acid. This reaction mixture was extracted with DCM, dried over magnesium sulfate, and evaporated to yield an oily product. The product was purified by silica gel open column chromatography and obtained Alexa-AC (**7**) (Scheme 1).

Preparation of the nanoparticles

PEG-4AC was prepared as described in our previous report.[16] Then we mixed the solution of 100 μL of 200 mg mL^{-1} PEG-4AC, 100 μL of 100 mg mL^{-1} fluorescent linker (Alexa-AC or PEG-Flu-3AC), 50 μL of 2 mg mL^{-1} physically encapsulated molecule (ferritin or trypsin or Dex-Flu or Dex-Mn), 25 μL of 0.1 M APS, and 25 μL of 0.1 M TEMED in 1 M Tris/HCl buffer in that order and then stirring the mixture for 20 min. After the reaction, the mixture was filtrated by Vivaspin 6–300 K (Sartorius, Germany) at 4000 rpm for 15 min at 4 °C.

Stability analysis of the dispersed nanoparticles

The nanoparticles were dispersed in the mice serum and stored at 37 °C for 12 h. Then the dispersed solution was filtrate by Vivaspin 6–300 K. Then supernatant and filtrate fractions were analyzed by means of dynamic light scattering (DLS) machine (Delsa™ Nano, Beckman Coulter, USA).

TEM observation

Transmission electron microscopy (TEM) images were obtained with an H-7000 electron microscope (Hitachi, Tokyo, Japan) operating at 75 kV. Copper grids (400 mesh) were coated first with a thin film of collodion and then with carbon. The nanoparticle dispersion (1 μL) was placed on the coated copper grids. The stained surface was dried at room temperature before observation.

AFM analysis

Atomic force microscopy (AFM) measurements were conducted by using NanoWizard II (JPK Instrument, Berlin, Germany) at

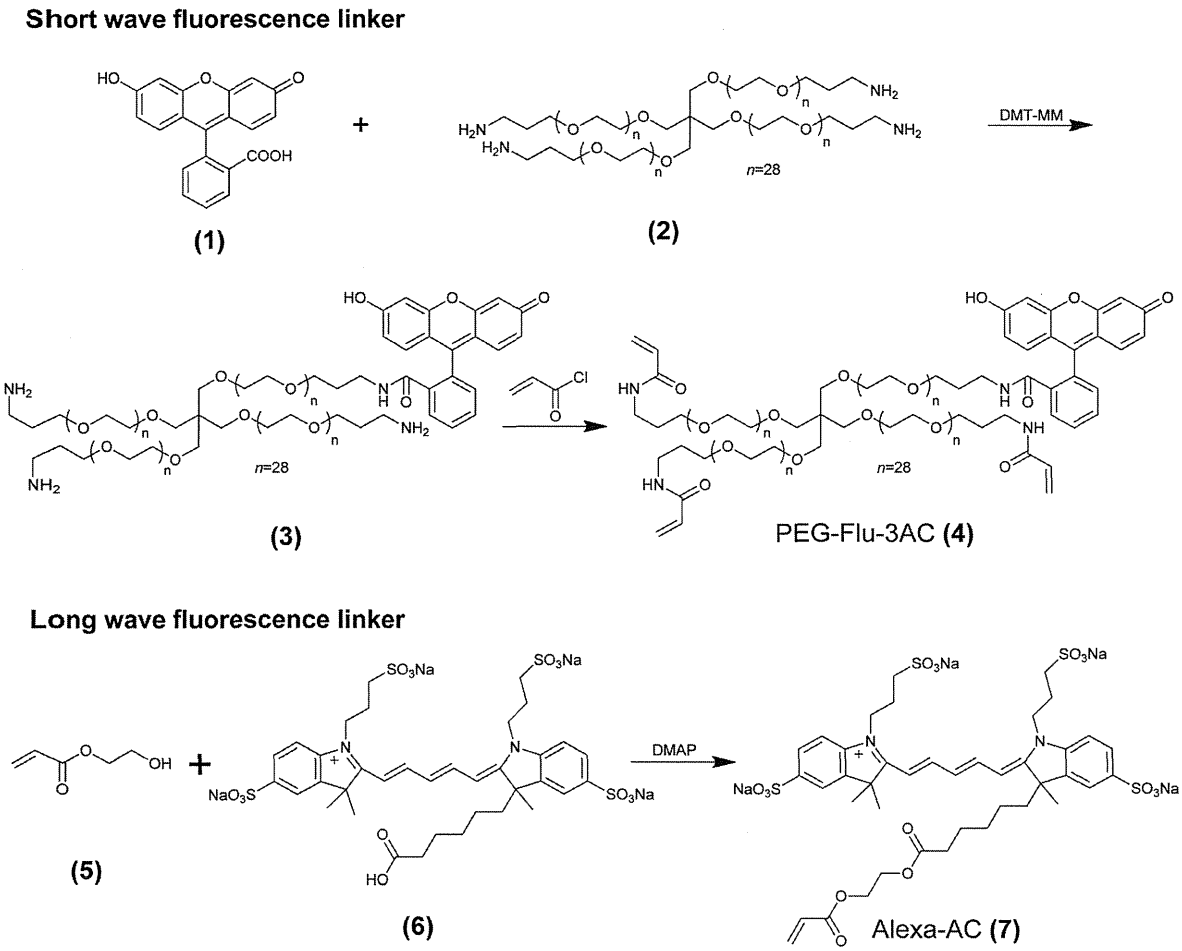

Scheme 1 Preparation procedures for the fluorescence labeled monomers.

room temperature. Images of nanoparticles were obtained in tapping mode using a commercial micro cantilever with a spring constant of 150 N m^{-1} (Olympus Corporation, Tokyo, Japan). AFM images were processed with JPK SPM image processing v.3 software.

In vivo animal study

Female BALB/c nude mice (Japan SLC, Shizuoka, Japan) used for *in vivo* experiments were maintained in accordance with the guidelines of the National Institute of Radiological Sciences (NIRS), and all experiments were reviewed and approved by the institute's committee for care and use of laboratory animals. Colon 26 murine cancer cells (RIKEN BioResource Center, Tsukuba, Japan) were cultured in Dulbecco's modified Eagle's medium (D5796, Sigma-Aldrich, St Louis, MO) supplemented with 10% fetal bovine serum, and incubated in a humidified atmosphere of 5% CO_2 in air at 37 °C. After suspension in phosphate-buffered saline, the cells were subcutaneously inoculated (1.0×10^6 cells/50 μL) into the left flank of the mice. When the tumor mass grew to 5–7 mm in average diameter about 10 days after inoculation, the tumor-bearing mice were used for the following *in vivo* experiments.

In vivo MR imaging of the nanoparticles

Magnetic resonance imaging (MRI) measurements were performed on a 7.0 Tesla horizontal magnet (Kobelco and Jastec, Tokyo, Japan) interfaced to a Bruker Avance I console (Bruker BioSpin, Etlingen, Germany) and controlled with ParaVision 4.0.1 (Bruker BioSpin).

The animal (BALB/c mice) were anesthetized using isoflurane 2.0% and held in a body cradle (Rapid Biomedical, Rimpar, Germany) in the prone position. Rectal temperature was continuously monitored and automatically controlled at 36.5 ± 0.5 °C using a nonmagnetic temperature probe (FOT-M and FTI-10, FISO Technology, Olching, Germany) and an electric temperature controller (E5CN, Omron, Kyoto, Japan) during measurements.

The tail vein was catheterized using a polyethylene tube (PE-10, Becton-Dickinson, Franklin Lakes, NJ) for nanoparticle injection. The mouse was then placed in a proton volume radiofrequency coil (35 mm inner-diameter, Bruker BioSpin) for transmission and reception previously warmed using a body temperature controller (Rapid Biomedical). The resonator units, including the mouse, were placed in the center of the magnet bore. Nanoparticle containing dextran-Mn was intravenously

injected to the mice through the polyethylene tubing line. The pharmacokinetics of the nanoparticles was repeatedly monitored by MRI measurements for 5 hours.

Two dimensional T1-weighted multi-slice spin echo MRI with fat suppression was performed with the following parameters: TR = 476 ms, TE = 9.57 ms, matrix size = 256 × 256, FOV = 3.2 × 3.2 mm^2, slice thickness (ST) = 1.0 mm, scan time 8 min 8 s, and number of acquisitions (NA) = 4. Slice orientation was horizontal (eight slices, gap 1 mm).

In vivo fluorescence imaging of nanoparticles

In vivo fluorescence imaging was performed before or 15, 30, 90, and 180 min after intravenous injection (100 μL) of Alexa 647-nanoparticle to the mice. Images were acquired using a fluorescent imager (Maestro EX, PerkinElmer) with the following parameters: excitation filter = 576–621 nm; emission filter = 635 nm longpass; acquisition setting = 630–800 nm in 10 nm steps; acquisition time = 100 ms; and FOV = 12.0 × 12.0 cm^2. Prior to and during the MRI scan, all mice were anaesthetized through a facemask with 2.0% isoflurane (Mylan Japan, Tokyo, Japan). The mice were put in a clean cage during the optical imaging and the urine was collected from the cage at the corresponding time. The mice were sacrificed after the 180 min-scanning and the main organs were collected, followed by measurement of their fluorescence by Maestro EX. After acquisition, unmixed fluorescence information was extracted from the fluorescence spectrum using the Maestro software package (PerkinElmer).

Results and discussion

Effect of encapsulated molecules on nanoparticle formation

First we prepared three types of nanoparticles containing dual probes: (1) nanoparticles with Alexa 647 and ferritin encapsulated chemically and physically, respectively; (2) nanoparticles with Flu and Dex-Mn encapsulated chemically and physically, respectively; and (3) nanoparticles with Flu and trypsin encapsulated chemically and physically, respectively. Fig. 1a shows the results of DLS diameter measurements of the three types of nanoparticles. Although the size distributions of these nanoparticles were different, the average diameters of these nanoparticles were all in the range of 150–300 nm. Since the encapsulation of the various probe molecules did not appear to substantially affect nanoparticle diameter, we concluded that our method could be used to prepare ~200 nm nanoparticles containing various compounds.

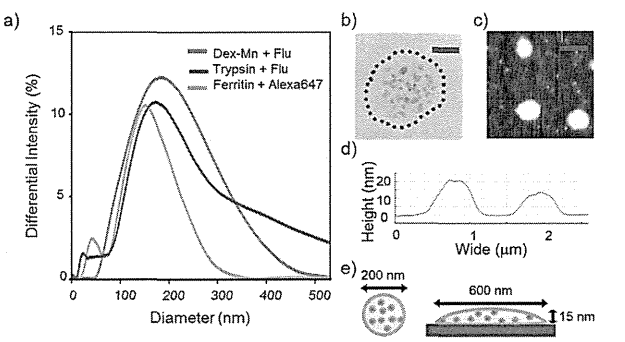

Fig. 1 (a) DLS measurements of the three types of nanoparticles prepared in this study, (b) TEM image of a nanoparticle containing ferritin, scale bar = 200 nm (c) AFM phase contrast image of the nanoparticles, scale bar = 1000 nm (d) cross-sectional topological profile obtained from image (c), and (e) schematic images of a nanoparticle dispersed in solution and of a nanoparticle affixed to a plate.

The diameter and shape of nanoparticles containing ferritin were examined by means of TEM and AFM (Fig. 1b and c). Interestingly, all the nanoparticles were observed to be round, with sizes in the range of 600–800 nm, which was 3 to 4 times the diameter measured by DLS (Fig. 1a). Three dimensional detailed AFM measurement showed the height of the nanoparticle was only 15–20 nm (Fig. 1d). This large difference in measured diameter probably occurred due to the different states of the nanoparticles required by these measurement techniques: the PEG-based nanoparticles were dispersed in water for DLS measurements, but were dried and affixed to a plate for TEM and AFM measurements. Because the nanoparticles were very soft and flexible, we expected that their shape likely would have changed during the drying pretreatment for TEM and AFM analysis. As shown in Fig. 1e, the volume of a spherical particle of 200 nm diameter, which was the diameter estimated by DLS analysis, is similar to the volume of a dried, flattened particle with a diameter of 600 nm and height of 15 nm, as estimated by TEM and AFM analysis. We determined that the black spots observed in the TEM image of the nanoparticles (Fig. 1b) corresponded to encapsulated ferritin; TEM images of particles that did not contain ferritin did not contain such black spots. The existence of the iron contained in ferritin was also confirmed by ICP-AES analysis (ESI, Fig. 1†). The image indicated that the encapsulated ferritin existed not only on the surface of the nanoparticles but also inside the nanoparticles.

Next, the stability of the nanoparticles was examined. Fig. 2a shows DLS measurements of a disperse solution of nanoparticles-encapsulated trypsin acquired just after preparation and the next day. The nanoparticles' diameter remained largely unchanged for 2 days of refrigerated storage in solution. This result indicates that the nanoparticles were stable under these storage conditions, and that they did not aggregate or collapse. Next, the stability of the probe molecules was examined by filtering solutions of two different types of nanoparticles, one with Flu chemically encapsulated and another with Dex-Flu physically encapsulated, and separately measuring the fluorescence intensity of the nanoparticle fraction and filtrate. We presumed that if the encapsulated Flu or Dex-Flu was leaked from the nanoparticles, the fluorescence signal of the filtrate would increase. Fluorescence intensities of the filtrate and nanoparticle fractions were measured after shaking for 12 h at 37 °C in mice serum. Although about 80% fluorescence signal was detected from the nanoparticle fraction, only a small signal was detected from the filtrates of both nanoparticle samples (Fig. 2b). The signals of the filtrate fraction of the chemically encapsulated nanoparticles were smaller than those of the physically encapsulated nanoparticles, presumably because the cleavage of the chemical bond to leak Flu into the filtrate was more difficult to achieve than the physical leak of Dex-Flu from

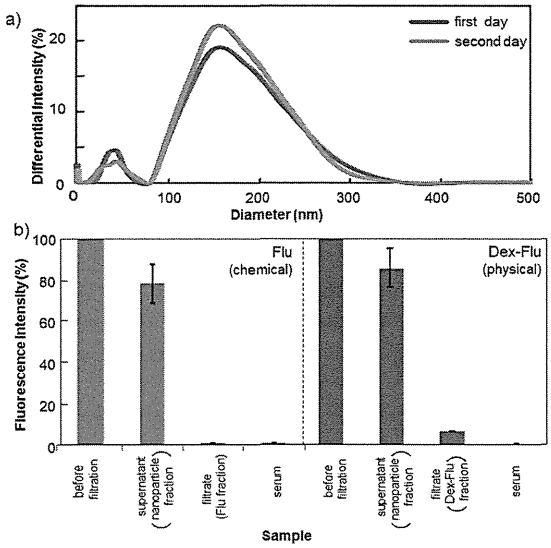

Fig. 2 (a) DLS measurements of a disperse solution of nanoparticles-encapsulated trypsin just after preparation and the next day, and (b) fluorescence analysis of nanoparticles modified either chemically (Flu, red bar) or physically (Dex-Flu, blue bar) with probe molecules after filtration.

its nanoparticles. The fluorescence intensity of the filtrate fractions was very small: the amounts of leaked Flu and Dex-Flu was negligible. These results indicate that both the nanoparticles and their encapsulated probe molecules were stable enough for further experiments.

Administration of nanoparticle-encapsulated Alexa 647 (chemically) and ferritin (physically) to mice

We used nanoparticles encapsulated with Alexa 647 and ferritin to study the nanoparticles' pharmacokinetics when administered to mice. Alexa 647, a fluorescent molecule with long excitation and emission wavelengths, is useful for monitoring the dynamics of nanoparticles within living mice. Because ferritin is an iron-storage protein that can be observed by TEM (Fig. 1b). It is a useful probe molecule for examining changes in the nanoparticles' shape upon excretion from the mice. The nanoparticles were administered *via* the mouse's coccygeal (tail) vein. The acute toxicity of the nanoparticles was negligible because no substantial changes in the blood pressure or heartbeat of the mice was observed after tail vein injection.

Although a strong fluorescence signal was detected in the bladder within 15 min of administration, no fluorescence signal was detected in other internal organs regardless of time, up to 180 min post-administration (Fig. 3a). The signal detected in the bladder increased with time, but disappeared after the mouse urinated (180 min). The collected urine was observed by TEM to observe excreted nanoparticles and ferritin (Fig. 3b). The shapes of the nanoparticles and the ferritin were similar to those observed in Fig. 1b. The distribution of ferritin within the nanoparticles (black dots in Fig. 3b) was similar to that observed prior to administration, as well. Therefore, we concluded that the nanoparticles had been excreted in the urine predominantly without changing form and without being

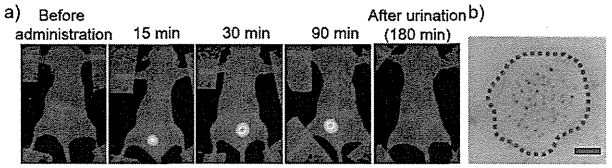

Fig. 3 (a) Fluorescence images of a mouse before and after administration of nanoparticles containing encapsulated ferritin and Alexa 647, and after urination, and (b) TEM image of a nanoparticle in mouse urine. Scale bar = 200 nm.

otherwise disturbed. In addition to containing clearly observable ferritin, the mouse urine also exhibited a fluorescence signal, demonstrating that both probes (ferritin and Alexa 647) remained within the nanoparticles when they were excreted. In general, nanoparticles less than 10 nm were excreted from urine,[17,18] however, nanoparticles with diameters greater than 10 nm are difficult to excrete in urine because the pore size of the kidney glomerulus is too small for penetration of these larger nanoparticles.[19] However, our results indicated that the 200 nm nanoparticles were excreted in urine; a similar phenomenon has been reported by He[20] and Lu,[21] who observed the excretion of 100 nm nanoparticles through mice urine. We hypothesized that the nanoparticles could change their shape to penetrate the kidney glomerulus, because the nanoparticles were very soft and flexible, as indicated by AFM images (Fig. 1c and d). More-detailed studies are needed to clarify the exact mechanism of excretion of the nanoparticles.

Administration of nanoparticle-encapsulated Flu (chemically) and Mn^{2+}-chelated compound (physically) to mice

Next, nanoparticles containing physically encapsulated Mn^{2+}-chelated compound and chemically encapsulated Flu were administrated to mice and were observed by means of MRI. MRI is a valuable diagnostic method for the observation of organs in living animals and humans,[22,23] and Mn^{2+} has recently received attention as an alternative MRI probe[24,25] because gadolinium (Gd^{3+}), the current standard MRI contrast agent, has been associated with nephrogenic systemic fibrosis.[26] On the other hand, low concentration of Mn^{2+} is considered as non toxic, because Mn^{2+} is an endogenous compound. To prevent leakage of Mn^{2+} from the nanoparticles, Mn^{2+} was chelated to dextran-modified diethylene triamine pentaacetic acid before being encapsulated in the nanoparticles.

An MRI signal (image contrast) was detected in the mouse bladder 15 min after administration (Fig. 4a, top row), and the signal increased with increasing time up to 5 h. MRI signals were also detected in the liver and kidney after administration (Fig. 4a, bottom rows). These results indicate that nanoparticles containing Mn^{2+} served as an effective positive MRI contrast agent, which is preferable for the detection of small changes that are caused by disease. For the liver and kidney, the MRI signals increased rapidly after administration and reached maximum intensities at 15 min after administration. Then, the signal started to decrease (Fig. 4b). The nanoparticles were eliminated from liver more rapidly than they were eliminated

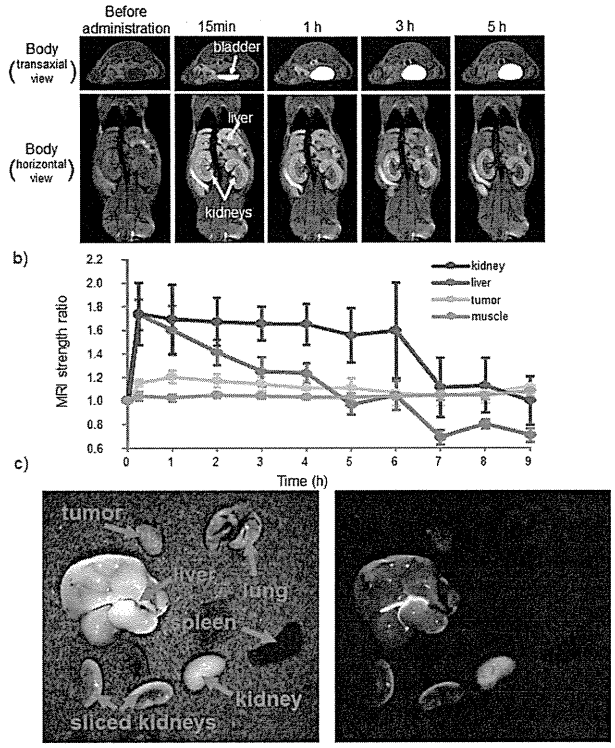

Fig. 4 (a) MRI images of a mouse before and after administration of nanoparticles containing encapsulated Mn^{2+} and Flu, (b) changes in MRI signal with increasing time post administration of the nanoparticles. The relative value was calculated from the equation (= MRI signal at the measured time/MRI signal before injection) (c) bright field and fluorescence images of organs 3 h after administration.

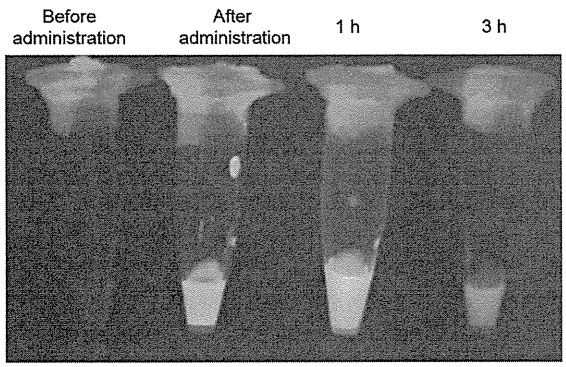

Fig. 5 Fluorescence images of urine collected from a mouse at different times before and after the administration of nanoparticles containing encapsulated Mn^{2+} and Flu.

from the kidneys. No obvious MRI signal enhancement was detected from other internal organs, including cancer tissue.

Although the fluorescence signal of Flu is hard to penetrate through the skin, the signal at *ex vivo* observation is more sensitive than an MRI signal. We therefore expected to see a small amount of nanoparticle accumulation in tissues or organs using *ex vivo* fluorescence analysis, after the *in vivo* study. The fluorescence signals of the internal organs and tissues of the mouse were analyzed 3 h after administration (Fig. 4c). Very strong fluorescence was observed in the bladder, and also a slight signal was observed in the liver and kidney; however, no signal enhancement was observed in the other organs such as cancer tissue, lungs, and spleen. This distribution of fluorescence signals corresponded with that observed for MRI signals in the same mouse, indicating that the two probes (Mn^{2+} and Flu) remained encapsulated within the nanoparticles and moved with the nanoparticles. Generally MRI is not highly sensitive for specific contrast agents (~μM), though it can be used to observe tissues deep within the body. On the other hand, fluorescence is highly sensitive *ex vivo* but cannot be used to observe tissues deep within the body. The combination of these two imaging techniques therefore can offer synergistic advantages over either modality used alone, and enables us to analyze the pharmacokinetics of nanoparticle distribution and excretion from the body in greater detail.

Strong fluorescence was detected from the urine that was collected from the mouse immediately after administration of the nanoparticles containing encapsulated Mn^{2+} and Flu (Fig. 5). This rapid excretion of nanoparticles in the urine was similar to the results observed for the nanoparticles containing ferritin and Alexa 647. (Fig. 3) Because both types of dual probes were excreted from the mice in a similar manner, we concluded that the composition of the encapsulated molecules did not affect the nanoparticles' distribution in, or rate of excretion from, the mouse's body. For this reason, we expect that a variety of probe molecules could be encapsulated within the soft PEG nanoparticles for use in animal experiments.

The nanoparticles were distributed mainly to the organs (bladder, kidney, and liver) that function to excrete dispensable or toxic compounds. Then, these nanoparticles were excreted quickly through the urine, along with the encapsulated probe molecules. Since the nanoparticles were excreted rapidly, the risk from compound where safety is a concern, like Gd^{3+}, will be reduced by encapsulation within the nanoparticles. In this report, we used non-targeting nanoparticles. It is expected that if active targeting of the nanoparticles to disease organs or tissues is achieved by the surface modification of the nanoparticle with targeting molecules (antibody, folate and so on) or changes to the nanoparticles size, the nanoparticles can be used as a theranostic tool.

Conclusions

In this study we developed a method to prepare soft PEG-based nanoparticles containing different probe molecules. The advantages of the nanoparticles were that (1) various probe molecules could be physically or chemically encapsulated within the nanoparticles, (2) different probe molecules were encapsulated within the nanoparticles simultaneously, (3) the nanoparticles could be detected in mice using various analytical techniques, depending on the type of probe molecules encapsulated, and (4) the soft nanoparticles were rapidly excreted through the urine, with low accumulation in the body. For these reasons, we concluded that these nanoparticles containing dual probes are promising for the reliable analysis of living animals.

Acknowledgements

We thank Dr S. Fukuda (UT), N. Nitta (NIRS), S. Shibata (NIRS), and S. Sakae (UT) for technical assistance with the TEM measurement, MRI measurement, for animal experiments, and for ICP-AES analysis, respectively. This work was supported by grants (Kakenhi) from the Ministry of Education, Culture, Sports, Science, and Technology (MEXT) of Japan, JSPS Core-to-Core Program, A. Advanced Research Networks, and the Naito Foundation. In addition, high-field MRI and optical imaging devices were supported by the Funding Program for World-Leading Innovative R&D on Science and Technology (FIRST Program).

References

1 J. Cheon and J.-H. Lee, *Acc. Chem. Res.*, 2008, **41**, 1630–1640.
2 L. E. Jennings and N. J. Long, *Chem. Commun.*, 2009, 3511–3524.
3 Y. Chang, Y. Li, X. Meng, N. Liu, D. Sun, H. Liu and J. Wang, *Polym. Chem.*, 2013, **4**, 789–794.
4 V. S. Talanov, C. A. S. Regino, H. Kobayashi, M. Bernardo, P. L. Choyke and M. W. Brechbiel, *Nano Lett.*, 2006, **6**, 1459–1463.
5 M. Higuchi, N. Iwata, Y. Matsuba, K. Sato, K. Sasamoto and T. C. Saido, *Nat. Neurosci.*, 2005, **8**, 527–533.
6 S. Mizukami, R. Takikawa, F. Sugihara, M. Shirakawa and K. Kikuchi, *Angew. Chem., Int. Ed.*, 2009, **48**, 3641–3643.
7 Y. Il Park, H. M. Kim, J. H. Kim, K. C. Moon, B. Yoo, K. Taek Lee, N. Lee, Y. Choi, W. Park, D. Ling, K. Na, W. K. Moon, S. H. Choi, H. S. Park, S.-Y. Yoon, Y. D. Suh, S. H. Lee and T. Hyeon, *Adv. Mater.*, 2012, **24**, 5755–5761.
8 J. Zhou, Y. Sun, X. Du, L. Xiong, H. Hu and F. Li, *Biomaterials*, 2010, **31**, 3287–3295.
9 A. B. Bourlinos, A. Bakandritsos, A. Kouloumpis, D. Gournis, M. Krysmann, E. P. Giannelis, K. Polakova, K. Safarova, K. Hola and R. Zboril, *J. Mater. Chem.*, 2012, **22**, 23327–23330.
10 A. Bumb, C. A. S. Regino and J. G. Egen, *Mol. Imaging Biol.*, 2011, **13**, 1163–1172.
11 S.-W. Chou, Y.-H. Shau, P.-C. Wu, Y.-S. Yang, D.-B. Shieh and C.-C. Chen, *J. Am. Chem. Soc.*, 2010, **132**, 13270–13278.
12 L. Shan, S. P. Wang, R. Sridhar, Z. M. Bhujwalla and P. C. Wang, *Mol. Imaging*, 2007, **6**, 85–95.
13 S. Murayama, B. Su, K. Okabe, A. Kishimura, K. Osada, M. Miura, T. Funatsu, K. Kataoka and M. Kato, *Chem. Commun.*, 2012, **48**, 8380–8382.
14 S. Murayama, T. Nishiyama, K. Takagi, F. Ishizuka, T. Santa and M. Kato, *Chem. Commun.*, 2012, **48**, 11461–11463.
15 S. Murayama, F. Ishizuka, K. Takagi, H. Inoda, A. Sano, T. Santa and M. Kato, *Anal. Chem.*, 2012, **84**, 1374–1379.
16 S. Murayama and M. Kato, *Anal. Chem.*, 2010, **82**, 2186–2191.
17 C. Eisner, H. Ow, T. Yang, Z. Jia, E. Dimitriadis, L. Li, K. Wang, J. Briggs, M. Levine, J. Schnermann and M. G. Espey, *J. Appl. Physiol.*, 2012, **112**, 681–687.
18 C. A. Simpson, K. J. Salleng, D. E. Cliffel and D. L. Feldheim, *Nanomed.: Nanotechnol., Biol. Med.*, 2013, **9**, 257–263.
19 M. Longmire, P. L. Choyke and H. Kobayashi, *Nanomedicine*, 2008, **3**, 703–717.
20 X. He, H. Nie, K. Wang, W. Tan, X. Wu and P. Zhang, *Anal. Chem.*, 2008, **80**, 9597–9603.
21 J. Lu, M. Liong, Z. Li, J. I. Zink and F. Tamanoi, *Small*, 2010, **6**, 1794–1805.
22 H. Kobayashi, S. Kawamoto, M. Bernardo, M. W. Brechbiel, M. V. Knopp and P. L. Choke, *J. Controlled Release*, 2006, **111**, 343–351.
23 A. B. Bourlinos, A. Bakandritsos, A. Kouloumpis, D. Gournis, M. Krysmann, E. P. Giannelis, K. Polakova, K. Safarova, K. Hola and R. Zboril, *J. Mater. Chem.*, 2012, **22**, 23327–23330.
24 A. C. Silva, J. H. Lee, I. Aoki and A. P. Koretsky, *NMR Biomed.*, 2004, **17**, 532–543.
25 I. Aoki, Y. J. L. Wu, A. C. Silva, R. M. Lynch and A. P. Koretsky, *NeuroImage*, 2004, **22**, 1046–1059.
26 H. S. Thomsen, *Radiol. Clin. North Am.*, 2009, **47**, 827–831.

BRAIN RESEARCH 1537 (2013) 350–355

Available online at www.sciencedirect.com

ScienceDirect

www.elsevier.com/locate/brainres

Brain Research

Research Report

Hemodynamic changes during neural deactivation in awake mice: A measurement by laser-Doppler flowmetry in crossed cerebellar diaschisis

Hiroyuki Takuwa[a], *Yosuke Tajima*[a], *Daisuke Kokuryo*[b], *Tetsuya Matsuura*[a,c], *Hiroshi Kawaguchi*[a], *Kazuto Masamoto*[a,d], *Junko Taniguchi*[a], *Yoko Ikoma*[a], *Chie Seki*[a], *Ichio Aoki*[b], *Yutaka Tomita*[e], *Norihiro Suzuki*[e], *Iwao Kanno*[a], *Hiroshi Ito*[a,*]

[a]*Department of Biophysics Program, Molecular Imaging Center, National Institute of Radiological Sciences, 4-9-1 Anagawa, Inage-ku, Chiba 263-8555, Japan*

[b]*Diagnostic Imaging Program, Molecular Imaging Center, National Institute of Radiological Sciences, 4-9-1 Anagawa, Inage-ku, Chiba 263-8555, Japan*

[c]*Academic Group of Mathematical and Natural Science, Iwate University, 4-3-5 Ueda, Morioka 020-8551, Japan*

[d]*Center for Frontier Science and Engineering, University of Electro-Communications, 1-5-1 Chofugaoka, Chofu, Tokyo 182-8585, Japan*

[e]*Department of Neurology, Keio University School of Medicine, 35 Shinanomachi Shinjuku-ku, Tokyo 160-8582, Japan*

ARTICLE INFO

Article history:
Accepted 18 September 2013
Available online 25 September 2013

Keywords:
Cerebellar blood flow
Red blood cell velocity
Red blood cell concentration
Neuronal deactivation
Awake animal
Crossed cerebellar diaschisis

ABSTRACT

Crossed cerebellar diaschisis (CCD) caused by contralateral supratentorial lesions can be considered a condition of neural deactivation, and hemodynamic changes in CCD were investigated with positron emission tomography (PET) in humans. In the present study, to investigate the effects of neural deactivation on hemodynamics, we developed a new mouse model of CCD, which was caused by middle cerebral artery occlusion (MCAO), and measured changes in cerebellar blood flow (CbBF), red blood cell (RBC) velocity and concentration due to CCD using laser-Doppler flowmetry (LDF) in awake mice. The ratio of the CCD side to the unaffected side in the cerebellum for CbBF 1 day after MCAO was decreased by −18% compared to baseline (before CCD). The ratio of the CCD side to the unaffected side for RBC concentration 1 day after MCAO was decreased by −23% compared to baseline. However, no significant changes in the ratio of the CCD side to the unaffected side were observed for RBC velocity. The present results indicate that the reduction of CbBF induced by neural deactivation was mainly caused by the decrease in RBC concentration. In contrast, our previous study showed that RBC velocity had a dominant role in the increase in cerebral blood flow (CBF) induced by neural activation. If RBC concentration can be considered an indicator of cerebral blood volume (CBV), hemodynamic changes due to neural activation and deactivation measured by LDF in mice might be in good agreement with human PET studies.

*Corresponding author. Fax: +81 43 206 0819.
E-mail address: hito@nirs.go.jp (H. Ito).

0006-8993/$ - see front matter © 2013 Elsevier B.V. All rights reserved.
http://dx.doi.org/10.1016/j.brainres.2013.09.023

1. Introduction

Positron emission tomography (PET) studies of the hemodynamics of crossed cerebellar diaschisis (CCD), which is caused by contralateral supratentorial lesions, have shown reductions in cerebral blood flow (CBF) and cerebral metabolic rate of oxygen ($CMRO_2$) in human (Lenzi et al., 1982; Martin and Raichle, 1983; Pantano et al., 1986; Yamauchi et al., 1992a, 1992b, 1999a, 1999b; Ito et al., 2002). CCD can be considered as neural deactivation (Ito et al., 2002), which is a reduction of neural activity as compared to the baseline level (spontaneous neural activity). In our previous study, we reported that hemodynamic changes in CCD measured with PET in humans showed almost the same degree of decrease in cerebral blood volume (CBV) and CBF (Ito et al., 2002). Animal studies, for which invasive procedures can be applied, can also be useful for investigating the mechanism of CCD resulting from neuronal deactivation. An anesthetized rodent model study reported the reduction of cerebellar blood flow (CbBF) associated with attenuation of spontaneous neural spiking activity, which was caused by middle cerebral artery occlusion (MCAO) and common carotid artery (CCA) occlusion (Gold and Lauritzen, 2002).

Recently, many investigators reported that anesthesia significantly affects the physiological states including the regulation of cerebral circulation throughout the brain (Martin et al., 2002, 2006; Lahti et al., 1999; Peeters et al., 2001; Sicard et al., 2003; Takuwa et al., 2011, 2012). Thus, we previously developed a system for measurement of cerebral hemodynamics in awake rodent using laser-Doppler flowmetry (LDF; Takuwa et al., 2011). Moreover, using this system, we investigated hemodynamic changes during neural activation in awake mice (Takuwa et al., 2012), and showed that the increase in red blood cell (RBC) velocity was far greater than that in RBC concentration and that it had a dominant role in the increase in CBF induced by neural activation.

On the other hand, hemodynamic changes caused by neuronal deactivation in awake animals was still unknown. To the best of our knowledge, no study has investigated the dynamics of RBC velocity and concentration independently in awake animals. In the present study, in order to investigate the effects of neural deactivation on hemodynamics, we developed a CCD mouse model caused by MCAO and measured changes in CbBF, a product of RBC velocity and concentration in cerebral microvessels, using LDF before and after neural deactivation under awake conditions.

2. Results

2.1. *Changes in CbBF and RBC velocity and RBC concentration during CCD*

Fig. 2 shows the percentage changes in the ratio of the CCD side to the unaffected side for CbBF and RBC velocity and concentration at one day after MCAO. The percentage changes in the ratio of CCD to the unaffected sides for CbBF, RBC velocity and concentration were $-18\pm11\%$, $5\pm14\%$ and $-23\pm17\%$, respectively. The percentage changes in the ratio of CCD to the unaffected sides for CbBF ($P<0.05$) and RBC concentration ($P<0.01$) were significantly lower than the ratios before MCAO (baseline), whereas no significant difference was observed in the ratio of CCD to the unaffected sides for RBC velocity between baseline and one day after MCAO (Fig. 2).

2.2. *Longitudinal measurement in hemodynamic response to CCD*

Longitudinal LDF measurement was performed for 2 weeks (Fig. 1). Before this experiment, we confirmed that CbBF and RBC velocity and concentration in intact animals (without MCAO but with attached cranial window) were quite stable for 14 days (data not shown). The percentage changes in the ratio of the CCD side to the unaffected side for CbBF at 7 days and 14 days after MCAO were $-18\pm8\%$ and $-21\pm11\%$, respectively (Fig. 2). The percentage changes in the ratio of CCD to the unaffected sides for RBC velocity at 7 days and 14 days after MCAO were $3\pm11\%$ and $-2\pm3\%$, respectively. The percentage changes in the ratio of CCD to the unaffected sides for RBC concentration at 7 and 14 days after MCAO were $-21\pm12\%$ and $-19\pm7\%$, respectively. The ratios of CCD to the unaffected sides for CbBF and RBC concentration at 7 and 14 days after MCAO were significantly lower than those at baseline ($P<0.01$). No significant difference was observed in CbBF and RBC concentration between 7 and 14 days after MCAO. No significant difference was observed in the ratio of CCD to the unaffected sides for RBC velocity throughout all measurements (Fig. 2).

2.3. *MRI measurement in MCAO*

The high intensity area in the cerebral cortical region of the MCAO side indicates infarction in the MCA territory in the T2-weighted image two weeks after MCAO for all mice (Fig. 3).

3. Discussion

We newly developed an awake mouse model of CCD (neural deactivation) caused by MCAO. Using these CCD model mice, the hemodynamic responses to neural deactivation including

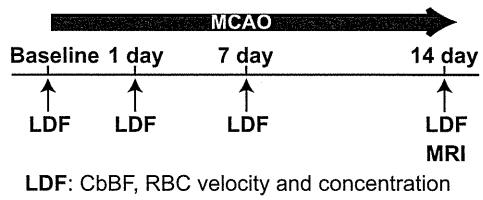

Fig. 1 – Experimental protocol for LDF measurement and MRI. LDF measurements were performed before (baseline) and 1, 7, and 14 days after MCAO. In each examination, changes in CbBF and RBC velocity and concentration were measured in both CCD side and unaffected side in awake mice. MRI experiments (T1-weighted imaging (T1WI) and T2-weighted imaging (T2WI)) were performed 14 days after MCAO.

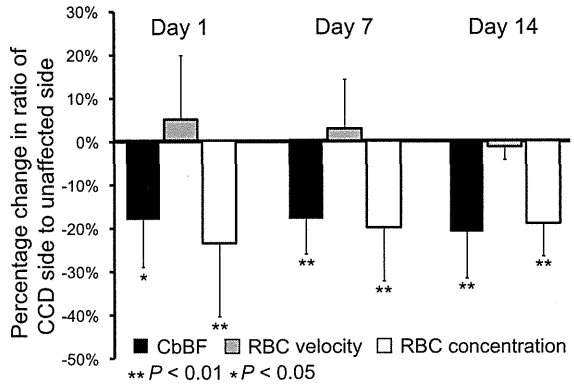

Fig. 2 – The percentage change in the ratio of CCD side to unaffected side for CbBF, RBC velocity and RBC concentration 1 day, 7 days and 14 days after CCD. Black, gray, and white bars indicate the percentage change in ratio of CCD to unaffected sides for CbBF, RBC velocity and RBC concentration, respectively. Error bars represent SD. (P<0.01 and *P<0.05).**

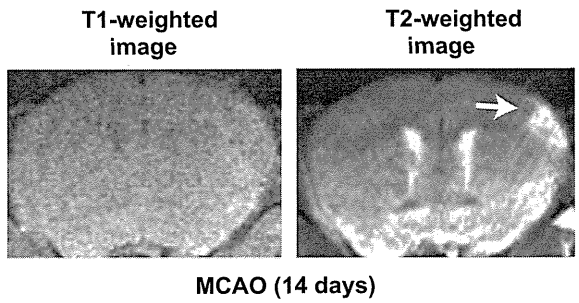

Fig. 3 – MRI experiments 14 days after MCAO. Left shows T1-weighted image. Right shows T2-weighted image. White arrow indicates the high intensity area in the T2-weighted image.

both RBC velocity and concentration were measured. This is the first observation of the effects of neural deactivation on the hemodynamics of awake mice. MRI examination showed the cerebral infarction in the unilateral cerebral cortex after MCAO (Fig. 3). The degree of decrease in CbBF caused by CCD remained almost the same throughout 2 weeks after MCAO. The reduction in RBC concentration was far greater than that in RCB velocity, suggesting that the change in RBC concentration played a dominant role in the reduction of CbBF under CCD. In human PET studies, CBF and CBV were significantly lower on the CCD side than the unaffected side, and the degree of difference between CBF of the two sides was almost the same as that between CBV. This resulted in there being no difference in vascular mean transit time (MTT), that is, the ratio of CBV to CBF, between the CCD and unaffected sides (Ito et al., 2002). This indicates that vascular blood velocity did not change during neural deactivation in the human PET study. If the RBC concentration can be considered an indicator of CBV, hemodynamic changes due to neural deactivation measured by LDF might be in good agreement with the PET measurement in humans previously reported (Ito et al., 2002).

The relationship between changes in RBC velocity and concentration due to a neural deactivation is opposite to that from a neural activation in which change in RBC velocity was seen to have a dominant role in increase in CBF (Takuwa et al., 2012). In a previous human PET study, the relationship between changes in MTT, the ratio of CBV to CBF, and CBV due to a neural deactivation (Ito et al., 2002) was opposite to that from a neural activation (Ito et al., 2005). These findings indicate the similarities between animal LDF studies and human PET studies under both neural activation and deactivation.

Our previous study confirmed that our apparatus could measure stable and reproducible CBF in awake mouse brain over a 1-week period (Takuwa et al., 2011). The present study also showed stable and reproducible CbBF, RBC velocity and concentration under CCD throughout a 2-week experimental period after MCAO. Therefore, we could conclude that the CCD model mice in this study could be used to investigate not only the mechanism of neural deactivation but also the long-term effects of CCD on neural and vascular function in brain using two-photon microscopy, animal PET and MRI.

The reason for the decrease in RBC concentration but the lack of change in RBC velocity under CCD is still unclear. According to Poiseuille's law, the flow of blood through a vessel is proportional to the fourth power of the vessel diameter; blood volume is proportional to the square of the diameter. Thus, $CBV = cCBF^{0.5}$ (c: constant; Ito et al., 2001, 2002, 2003). Based on this equation, the degree of change in CBV associated with a decrease in CBF during neural deactivation is higher than in CBV associated with an increase in CBF during neural activation. The relationship between CBF and CBV in this equation can explain the results of human PET studies in neural activation (Ito et al., 2005) and neural deactivation (Ito et al., 2002). Therefore, we previously hypothesized that hemodynamic changes in neural activation and deactivation are based on Poiseuille's law (Ito et al., 2002). The present study as well as the previous study in neural activation using LDF (Takuwa et al., 2012) shows the same tendency as those human PET studies.

Yamauchi et al. (1999a, 1999b) previously reported that CCD caused by unilateral supratentorial infarction showed a reduction of hematocrit in the CCD side of the cerebellum in a human PET study. Although we did not confirm decreased hematocrit in the CCD side in this model mouse, the reduction of RBC concentration in the CCD side might be associated with not only a decrease in CBV but also a reduction in hematocrit.

The regulatory mechanism of CbBF in the CCD side must be associated with several factors. Gold and Lauritzen (2002) showed that reduced neuronal activity in the cerebral cortex leads to a decrease in spontaneous Purkinje cell spike activity in the contralateral cerebellar hemisphere using anesthetized CCD model rat. It is possible that the attenuation of spontaneous neural activation in cerebellum caused a decrease in synthetase of a vasoactive mediator in neurovascular coupling (e.g., nitric oxide (NO), cyclooxygenase-2 (Cox-2) and adenosine) released from neurons and glia by neural activity (Yang et al., 2003; Bakalova et al., 2002; Ko et al., 1990). To explore the mechanism, further experiments using synthetase inhibitors or immunostaining techniques in mice will be